

# Tumor Heterogeneity in VHL Drives Metastasis in Clear Cell Renal Cell Carcinoma

**Junhui Hu**

University of California Los Angeles <https://orcid.org/0000-0001-9260-2858>

**Ping Tan**

West China Hospital of Sichuan University

**Moe Ishihara**

University of California Los Angeles

**Nicholas Bayley**

University of California, Los Angeles

**Shiruyeh Schokrpur**

University of California, San Diego

**Jeremy Reynoso**

University of California, Los Angeles <https://orcid.org/0000-0002-4376-0101>

**Parmjit Jat**

MRC Prion Unit at UCL / Institute of Prion Diseases

**Jacques Van Snick**

Ludwig Institute for Cancer Research

**Beatrice Knudsen**

University of Utah <https://orcid.org/0000-0002-7589-7591>

**Arnold Chin**

University of California Los Angeles

**Robert Prins**

University of California, Los Angeles <https://orcid.org/0000-0002-6282-6583>

**Thomas Graeber**

University California Los Angeles <https://orcid.org/0000-0001-8574-9181>

**Hua Xu**

Tongji Hospital, Tongji Medical College, Huazhong University of Science and Technology

**Lily Wu** (✉ [lwu@mednet.ucla.edu](mailto:lwu@mednet.ucla.edu))

University of California Los Angeles

---

**Article**

**Keywords:** VHL gene deletion, EMT, intratumoral heterogeneity, ccRCC, metastasis, periostin, paracrine crosstalk

**Posted Date:** September 10th, 2021

**DOI:** <https://doi.org/10.21203/rs.3.rs-846239/v1>

**License:**  This work is licensed under a Creative Commons Attribution 4.0 International License.

[Read Full License](#)

---

# Abstract

To study the impact of intratumoral VHL heterogeneity observed in patient ccRCC primary tumors, we engineered VHL gene deletion in three RCC models, including a new primary tumor cell line derived from an aggressive metastatic ccRCC. The VHL gene-deleted (VHL-KO) cells underwent epithelial-to-mesenchymal transition (EMT) and showed diminished proliferation and tumorigenicity compared to the parental, VHL-expressing (VHL+) cells. Renal tumors with either VHL+ or VHL-KO cells alone exhibit minimal metastatic potential. Interestingly, tumors with both cells displayed rampant lung metastasis, highlighting a novel cooperative metastatic mechanism. The poorly proliferative VHL-KO cells stimulated the proliferation, EMT and motility of neighboring VHL+ cells. We found that periostin (POSTN), a protein product overexpressed and secreted by VHL- cells, promoted metastasis by enhancing the motility of VHL-WT cells and facilitating vascular escape of tumor cells. Genetic deletion or antibody blockade of POSTN dramatically suppressed lung metastases in our preclinical models. Our work suggests a new strategy to halt progression in ccRCC by disrupting the critical metastatic crosstalk between heterogeneous cell populations within a tumor.

## Introduction

Renal cell carcinoma (RCC) is the most common cancer of the kidney, consistently ranking amongst the top ten most prevalent malignancies in the world. Annually diagnosed cases exceed 70,000 in the US and 350,000 worldwide<sup>1</sup>. RCC arises from the epithelial cells of the renal cortex and is characterized by a wide range of histological subtypes with variable clinical behaviors. The clear cell subtype of RCC (ccRCC) constitutes more than 70% of RCC, and features tumor cells with clear, lipid-laden cytoplasm. Patients with localized disease are treated with nephrectomy and have a favorable 5-year survival of 73%. Unfortunately, approximately 30% of patients develop metastatic disease, frequently spreading to the lung<sup>2</sup>. Despite the development of new targeted therapies, patients with metastatic ccRCC still have a poor outcome with a median progression free survival of 15.1 months using a combined therapy of axitinib and pembrolizumab<sup>3</sup>.

Detailed studies of von Hippel Lindau (VHL) disease (a rare hereditary cancer syndrome manifesting as renal, CNS, adrenal, and pancreatic tumors) led to the identification and cloning of the *VHL* tumor-suppressor gene<sup>4,5</sup>. VHL also plays an integral role in the pathogenesis of sporadic, non-familial ccRCC, as somatic mutations of VHL have been reported in as many as 90% of cases<sup>6-10</sup>. Seminal research over the past two decades has unraveled the VHL protein's intricate and important function as an E3 ubiquitin ligase that targets the alpha subunit of hypoxia-inducible transcription factors (HIF- $\alpha$ s) for oxygen-dependent degradation<sup>11,12</sup>. Although constitutive activation of the HIF pathway due to VHL loss has been implicated as an oncogenic driver<sup>13,14</sup>, the precise oncogenic mechanism of VHL loss remains elusive. Numerous mouse models of renal-tubule-targeted *VHL* deletion have failed to generate renal lesions beyond preneoplastic cysts, even when combined with deletion of other tumor suppressor genes such as PTEN or p53<sup>15-19</sup>. It is clear that the loss of VHL function upregulates both HIF1a and

HIF2a, however these two paralogs appear to have distinct, and often contrary, roles in their gene regulatory activities<sup>20,21</sup>. Recent research suggests that HIF2a plays an oncogenic role, whereas HIF1a suppresses ccRCC tumors<sup>22</sup>. These opposing oncogenic roles remain an area of active debate<sup>23-25</sup>.

The potential contribution of VHL loss and its downstream effectors to metastatic progression is also poorly defined, as there is no significant correlation between *VHL* mutational status and clinical outcome<sup>26</sup>. We and others have reported that silencing or deleting the *VHL* gene consistently results in epithelial-to-mesenchymal transition (EMT)<sup>27-29</sup>. EMT is an embryonic program used by polarized epithelial cells to break away from cell-cell contacts and basement membrane attachment, enabling cellular migration to distant sites<sup>30</sup>. It is highly reminiscent of the process that carcinomas adopt during metastatic spread<sup>31</sup>, although the direct role of EMT in cancer metastasis is actively debated<sup>32,33</sup>.

Our *VHL*-deleted ccRCC models revealed a new concept: EMT contributes to metastatic dissemination, but indirectly. Specifically, inactivation of VHL renders VHL<sup>-</sup> tumor cells highly motile but non-proliferative. Yet, these VHL<sup>-</sup> cells drive metastasis by producing key soluble factors, including periostin (POSTN), which disrupts the vasculature and induces dissemination and growth of VHL-expressing (VHL<sup>+</sup>) cells. This cooperative mechanism of metastasis, which occurs as a result of interactions between two distinct cell populations, highlights the active role of intratumoral heterogeneity in cancer aggression. A better understanding of the signals that mediate these interactions could identify novel therapeutic interventions to halt the deadly metastatic spread of ccRCC.

## Results

### Intratumoral heterogeneity in VHL expression is prevalent in ccRCC

The mutation or inactivation of the VHL gene is recognized as a trunk lesion in the majority of ccRCC cases<sup>9</sup>. However, it is unclear whether *VHL* loss or inactivation is uniform throughout the entire tumor. VHL protein expression was analyzed by immunohistochemical analyses (IHC) of large tissue sections of a total of 26 ccRCC cases, collected by surgical resection at our institution over the past five years (Table 1, Supplemental Figure 1A). The most recent 10 cases (#17 to 26) were freshly harvested tumor specimens collected from consecutive surgeries performed by a single surgeon (Table 1 and Supplemental Figure 1B). Intratumoral heterogeneity in VHL protein expression was commonly observed as none of the ccRCC cases displayed a uniform loss of VHL throughout the entire tumor (Table 1 and Supplemental Figure 1A). Representative images of H&E and VHL stains of consecutive cases, #20, 21, 22, and 23, are shown in Figure 1A, 1B, 1C and 1D. Case #20 contained the least amount of VHL positivity of 10%, while case #23 is a benign oncocytoma that is uniformly VHL positive.

To investigate *VHL* and other oncogenic mutations of ccRCC in detail, we established primary tumor cell lines and patient-derived xenografts (PDXs) in chorioallantoic membrane (CAM) model from freshly harvested surgical specimens (cases #18-26). The rate of PDX engraftment in CAM is efficient at an 80% success rate<sup>34</sup>. Here, we focused on the most aggressive case of metastatic ccRCC, case #22 (Table

1). This patient presented with a 10-cm, Fuhrman grade 4, primary tumor and bilateral lung metastases and succumbed to the disease within one year of nephrectomy despite multiple surgical and pharmacological interventions. As shown in Figures 1C, VHL expression in the primary tumor of #22 was highly heterogeneous, with VHL<sup>+</sup> cells juxtaposed to VHL<sup>-</sup> cells. The CAM PDXs established from small tumor pieces of the primary tumor from case #22 revealed the presence of intermixed VHL<sup>+</sup> and VHL<sup>-</sup> tumor cells (Supplemental Figure 1C). We successfully generated a primary tumor cell line from case #22, which consisted an equal mixture of VHL<sup>+</sup> and VHL<sup>-</sup> tumor cells upon initial tumor dissociation (P0). However, only the VHL<sup>+</sup> tumor cells were able to propagate continually, up to passage 20 currently (data not shown). Whole exome sequencing (WES) showed that this #22 cell line shared more than 80% of COSMIC annotated mutations found in the parental tumor (Supplemental Figure 1D). The *VHL* gene sequence of the #22 cell line possessed a homozygous in-frame T506C transition, leading to a L169P amino acid substitution (Supplemental Figure 1E). L169P is a common variant, with 14 occurrences in 446 patients analyzed<sup>35</sup>. However, it has not been biochemically characterized and its effect on VHL function is unknown. Our preliminary studies showed this L169P variant is comparable to wildtype VHL in its protein stability and in its ability to degrade HIF1a protein in an oxygen dependent manner (Supplemental Figure 1F, 1G, 1H, 1I). Common ccRCC driver mutations (such as *VHL*, *TP53*, *BAP1*, *PBRM1*, and *SETD2*) were analyzed by WES of four different tumor areas of the primary #22 tumor and compared to its derivative cell line as shown in Figure 1E. Variant allele frequencies (VAFs) and copy number ratios (CNR) showed clonal missense mutations in the *VHL* gene and frameshift mutations in the *BAP1* gene in the #22 cell line (Figure 1E). However, these two mutations were subclonal with varying contributions in the four tumor areas, suggesting cellular heterogeneity within the primary tumor.

Next, we analyzed single cell sequencing of primary tumor tissue and dissociated primary tumor cells from case #22. Heterogeneous VHL positivity was confirmed and is shown in Figure 1F and 1G, which cross-validates the VHL staining in Figure 1C demonstrating both VHL positive and VHL negative populations in the primary tumor. Next, we utilized the TCGA database to further investigate VHL heterogeneity. The CNR at the *VHL* locus was analyzed in the TCGA KIRC (Kidney Renal Clear Cell Carcinoma) cohort (n = 459) after adjusting for both tumor purity and ploidy. The peak CNR value (average for the mixture of cells analyzed) was between -1.1 and -0.4, suggesting that many purity and ploidy corrected TCGA samples had subclonal, single-copy loss of *VHL*, as a value of -1.1 represents a two-copy loss and -0.4 represents one-copy loss (shown as the dotted lines, Figure 1H). The VAFs of somatic *VHL* mutations in the TCGA KIRC cohort (n = 148) after adjusting for both tumor purity and ploidy also displayed a wide spectrum spanning between 0.5 and 1, indicating subclonal mutations (Figure 1I). These results use consensus purity and ploidy estimates from three computational algorithms and IHC analysis (see Methods). We further validated that consistent evidence of subclonal VHL copy number loss and mutation can be found after adjusting with only one of the computational measures of tumor purity (ABSOLUTE) (Supplemental Figure 1J and 1K).

Collectively, IHC and genomic profiling indicates that VHL protein expression and gene mutation is heterogenous within individual human ccRCC tumors.

## Metastasis requires cooperation between VHL-KO and VHL-WT RCC cells

To study the functional interaction between VHL<sup>+</sup> and VHL<sup>-</sup> RCC cells, we used the CRISPR/Cas9 system to delete the *VHL* gene in the murine RCC RENCA (RC) and human ACHN cell line as previously reported<sup>36</sup> and in the primary cell line #22 here. The first *VHL*-deleted RENCA line (denoted as RVN) was created by transducing RC cells with *VHL*-targeted lentiCRISPR (29). RVN cells underwent EMT and developed rampant lung metastases upon intrarenal implantation and were much more aggressive than the parental RENCA cells<sup>36</sup>. Unexpectedly, lung metastases from RVN tumors consisted largely of VHL-expressing cells with minor pockets of *VHL*-deleted, MMP-9<sup>+</sup> cells (Supplemental Figure 2A). This result alerted us to the non-clonal nature of RVN line and that both VHL positive and negative cells are required to produce metastasis. We therefore selected several clones with bi-allelic *VHL* gene deletion, generated through transient expression of CRISPR/Cas9 as described in Hu et al.<sup>36</sup>. The clonal *VHL*-knockout line is denoted as RC-VHL-KO, and the parental, VHL<sup>+</sup> control treated line is denoted as RC-VHL-WT.

Next, we established renal tumors with either RC-VHL-WT cells, RC-VHL-KO cells, or a 1:1 mixture of the two cell lines. The growth and dissemination of these tumors in mice were monitored by bioluminescence imaging (BLI) of the firefly luciferase marker gene. RC-VHL-WT and mixed primary tumors grew well, but VHL-KO tumors barely grew (Figure 2A, B). Interestingly, the mixed tumor bearing mice exhibited prominent thoracic metastatic BLI signals (Figure 2A, C). These mice also suffered tumor cachexia with significant weight loss (Supplemental Figure 2B). Lung metastasis was not observed in the VHL-KO tumor group (Supplemental Figures 2C). Detailed histological analyses revealed the mixed-tumor group exhibited greatly increased numbers and sizes of lung metastases compared to the VHL-WT tumor group, which could be easily appreciated even at low magnification (Figure 2D)<sup>36</sup>. The in vivo growth and metastatic behavior of the RC tumors were further verified in the avian chorioallantoic membrane (CAM) tumor system<sup>37,38</sup>. The CAM model substantiated the poor growth of VHL-KO tumors in comparison to VHL-WT and 1:1 mixed tumors (Figure 2E). Although the mixed tumors exhibited an insignificant reduction in tumor size compared to VHL-WT tumors, they demonstrated a significant increase in circulating tumor cells, reflecting the heightened metastatic potential of the mixed tumors (Figure 2F).

Next, we ascertained whether this novel cooperative mechanism of metastasis could be operating in human ccRCC models. The same CRISPR/Cas9 lentiviral system was employed to knock out the *VHL* gene in the human ACHN (AC) cell line (29, 34), a widely used human RCC cell line known to express wildtype VHL protein<sup>39</sup>. Consistent with the findings in the RC model<sup>29</sup>, the clonal AC-VHL-KO line exhibited an EMT cellular morphology (Supplemental Figure 2D), elevated expression of EMT markers (Supplemental Figure 2E). Tumors derived from both AC-VHL-WT and 1:1 VHL-WT:VHL-KO cells grew well after intrarenal implantation (Figure 2G). However, when assessed by gross tissue inspection and detailed histology, lung metastases were observed only in the mixed-tumor group (Figure 2G). Of note,

the AC cells grew more slowly than RC cells in mice, resulting in smaller primary tumors and lung metastases.

The same CRISPR/Cas9 approach was applied to the VHL<sup>+</sup> primary tumor cells of case #22 to generate a VHL-deleted derivative line, #22 VHL-KO, denoting the engineered knockout of VHL gene. The gene edited biallelic frameshift mutation in #22 VHL-KO cells were confirmed by DNA sequencing (Supplemental Figure 1E). CAM tumors were established for #22 VHL<sup>+</sup> primary cells, #22 VHL-KO or 1:1 mixture of these 2 cell types (Supplemental Figure 2F). Importantly, the metastatic potential of the #22 CAM tumors, assessed by presence of tumor cells in the chick embryo, was only significantly increased in the mixed tumor group (Figure 2H), paralleling the findings of RC and AC model. Further analyses of differential single cell gene expression in VHL-KO/VHL<sup>+</sup> cells for these three models, #22, ACHN and RENCA, showed a congruent 200-geneset pattern of up- and down-regulation for a wide spectrum of genes (Figure 2I). Similar congruent patterns in functional enrichments, such as sumoylation of transcription factor, and depletions, such as wnt signaling pathway and apoptotic cleavage of cellular proteins, were also observed across ccRCC cells from the different sources (Figure 2J).

Collectively, the data from the VHL-deleted ccRCC models, #22, ACHN and RENCA, revealed that the cooperative interactions between two distinct populations of tumor cells (VHL<sup>-</sup> and VHL<sup>+</sup> cells) are required to produce distant metastases.

### **VHL<sup>-</sup> or VHL-KO cells induce the proliferation of VHL<sup>+</sup> tumor cells**

An immediate question raised by the cooperative metastatic models (Figure 2) is the nature of the crosstalk between the two cell populations leading to induction of metastasis. We and others have reported that VHL gene deletion causes RCC tumor cells to undergo EMT<sup>29</sup> and slow proliferation, as VHL-KO cells derived from the murine RC<sup>36</sup> or the human AC (34) models grew slower than their parental VHL-WT cells in cell culture (Figure 3A, B) and in vivo (Figure 2A, B, E). The primary cells of #22 also displayed the same growth pattern with the #22 VHL-KO grew significantly slower than the parental VHL<sup>+</sup> cells (Figure 3C). In transwell co-cultures, the presence of VHL-KO cells induced the proliferation of VHL<sup>+</sup> or VHL-WT cells in all 3 models, suggesting the influence of soluble or paracrine factors (Figure 3A, D and E). Cellular proliferation assessed by the rate of Ki67 staining was greater than 3 times higher in the VHL-positive (31.4%) than the VHL-negative areas (7.8%) of the 1:1 mixed RC renal tumor (Figure 3F) and lung metastases (Supplemental Figure 3A). Analysis of human ccRCC tumor #22 revealed the same pattern, with Ki67 positivity rate more than 7 times higher in the VHL-positive (26.6%) than the VHL-negative tumor areas (1.4%) (Figure 3G). The HALO infiltration analysis module was applied to decipher the spatial relationship between the different cell populations. The highest concentration of Ki-67<sup>+</sup> cells resided at the edges of VHL<sup>+</sup> areas that were in closest proximity to and under the greatest potential paracrine influence of the VHL<sup>-</sup> cells (Figure 3H). This is consistent with the in vitro findings that VHL<sup>-</sup> cells are promoting the proliferation of VHL<sup>+</sup> cells.

If inducing cellular proliferation of VHL<sup>+</sup> tumor cells is a critical metastasis-promoting function of the VHL<sup>-</sup> cells, then metastatic lesions would be expected to be dominated by VHL<sup>+</sup> cells. In fact, this is the precise finding in lung metastases of RC model and case #22. The high prevalence of VHL<sup>+</sup> cells was observed in large lung metastases (Figure 3I) and very small metastatic lesions (Figure 3J) of 1:1 mixed RC tumors, and was assessed to exceed 95% (Figure 3K), respectively by IHC, immunofluorescent staining (IF) and flow cytometry. The dominant presence of VHL-WT cells in the very small metastatic lesion suggested that the expansion and intravasation of VHL-WT cells occurred early in the metastatic cascade (Supplemental Figure 3B). Paralleling the preclinical scenario, histological analyses of the lung metastases of case #22 showed a high prevalence of VHL<sup>+</sup> cells, far exceeding the ratio of VHL<sup>+</sup>/VHL<sup>-</sup> cells in the primary tumor (Figure 3L, 3M and Table 1).

Collectively, our preclinical and clinical findings suggest that VHL-KO or VHL<sup>-</sup> tumor cells drive the cooperative metastasis by inducing proliferation of VHL-WT or VHL<sup>+</sup> cells.

### **VHL-KO cells induce the EMT and the motility of VHL-WT tumor cells**

The deletion of *VHL* gene consistently induced the EMT program in VHL-KO RCC models as previously reported<sup>29</sup>, manifested in mesenchymal cell morphology, elevated EMT gene expression, and a prominent increase in cell motility (29, 34). We reasoned that a pro-metastatic paracrine influence of VHL-KO cells could also induce EMT and motility of the VHL-WT cells. Coculture of RC-VHL-KO cells and RC-VHL-WT cells led to upregulation of EMT markers such as *N-Cad*, *MMP-9*, and *SMA* and downregulation of the epithelial marker *E-Cad* in the RC-VHL-WT cells (Figure 4A). We measured the motility of mStrawberry-labeled RC-VHL-WT or EGFP-labeled RC-VHL-KO cells alone (Figure 4B) or in cocultures (Figure 4C) using time-lapse live-cell microscopy. VHL-KO cells migrated much faster than VHL-WT cells (Figure 4D and Supplementary Videos 1A, 1B, 1C, and 1D), and the migration of VHL-WT cells was greatly enhanced in coculture with VHL-KO cells (Figure 4D). We further performed the migration assay in a 3D system allowing cancer cells to migrate through an extracellular matrix. Paralleling the results of the 2D system, VHL-KO cells also migrated faster than VHL-WT cells in 3D (Supplemental Figure 4A and Supplementary Videos 2A, 2B, 2C, and 2D). Conditioned medium from VHL-KO cells was also able to enhance the motility of VHL-WT cells, albeit to a lesser extent than coculture (Figure 4E and Supplementary Video 3). Together, these results show that EMT<sup>+</sup> VHL<sup>-</sup>KO cells are able to increase the proliferation and the motility of neighboring VHL-WT cells via soluble factors and cell-cell contact, promoting the aggressive, metastatic behavior of the tumor.

### **Periostin is a soluble factor secreted by VHL-KO cells that promotes metastasis**

Next, we sought to clarify the signals downstream of VHL loss that could be governing metastasis. RNA sequencing identified four HIF1 $\alpha$ -regulated genes that are coordinately upregulated upon *VHL* gene

deletion and that predicted a very poor patient survival in the TCGA RCC (KIRC) database<sup>29</sup>. Amongst the four identified HIF1a-regulated genes, we focused on POSTN because it encodes a secreted cell-adhesion protein upregulated in EMT with known paracrine activity that confers aggressive and metastatic behavior<sup>40,41</sup>. POSTN is upregulated in kidney cancer<sup>42</sup> and is a poor prognostic indicator for RCC (Supplemental Figure 5A). However, the functional role of POSTN in RCC tumorigenesis has not been defined. POSTN was upregulated in RC-VHL-KO relative to RC-VHL-WT cells at the RNA (Supplemental Figures 5B) and protein level (Figure 4F), and it was HIF1a dependent as deletion of HIF1a gene significantly reduced POSTN RNA level (Supplemental Figure 5C). A compound deletion of *VHL* and *HIF1a* can mitigate the motility promotion effect as shown Supplemental Videos 4A and 4B. To assess the contribution of POSTN to cell motility, we constructed a *VHL* and *POSTN* double-gene knockout line (RC-VHL/POSTN-KO) and showed that this line also exhibited significantly decreased augmentation of VHL-WT cells' motility (Figure 4G and Supplementary Videos 5A and 5B). To further pinpoint the role of POSTN as the soluble mediator of enhanced cell motility, we employed a monoclonal anti-POSTN neutralizing antibody (MPC5B4) that disrupts the interactions between POSTN and integrin  $\alpha\text{V}\beta\text{3}$ <sup>43</sup>. The POSTN-blocking antibody abrogated VHL-KO cells' stimulation of VHL-WT cells' motility (Figure 4H and Supplementary Videos 6A and 6B).

The mechanism of action of POSTN was further investigated with add-back experiments. The addition of recombinant POSTN to VHL-WT cells significantly promoted their motility, which was blocked by the cyclic-peptide integrin inhibitor, cilengitide (Figure 4I and Supplemental Figure 5D). The addition of recombinant POSTN to VHL-WT cells activated focal adhesion kinase (FAK) via phosphorylation at Tyr 397, which was blocked by cilengitide (Figure 4J). In RC-VHL-WT and RC-VHL-KO coculture, cilengitide disrupted the enhanced motility of VHL-WT cells in a dose dependent manner (Figure 4K and Supplementary Videos 7A, 7B, 7C and 7D). These findings from our preclinical model suggested that POSTN secreted by the VHL-KO cells could be an important mediator of the cooperative metastatic mechanism. Hence, it is critical to verify the correlation of VHL loss with the upregulation of POSTN expression in ccRCC human tumors.

As shown in Figure 5A, POSTN colocalized with RC-VHL-KO cells but not with RC-VHL-WT cells in serial sections of a large metastatic lesion from a mixed RENCA tumor. IHC of VHL and POSTN in serial sections of primary tumor of case #22 (Figure 5B) showed that VHL<sup>+</sup> areas were POSTN<sup>-</sup> whereas VHL<sup>-</sup> areas stained positive for POSTN (Figure 5C). Furthermore, quantitative analysis of VHL<sup>+</sup>POSTN<sup>-</sup> and VHL<sup>-</sup>POSTN<sup>+</sup> cells in this case #22 using the HALO image analysis software confirmed the distinct spatial distribution of these two populations (Figures 5D). IF staining of the lung metastatic lesions of case #22 clearly showed the predominance of VHL<sup>+</sup> cells (red fluorescence), which were excluded from the POSTN<sup>+</sup> cells (green fluorescence, Figure 5E). This reciprocal relationship was further confirmed in the retroperitoneal lymph node metastasis of case #17 (Figure 5F, Table I). The increased RNA expression of POSTN upon VHL knockout in #22 primary cells was further validated by qRT-PCR (Figure 5G). Analysis of the VHL and POSTN expression pattern in a tissue microarray (TMA) constructed from over 300 ccRCC patients who underwent nephrectomy at our institution<sup>44</sup>, confirmed the reciprocal

relationship in approximately 30% of cases (Supplemental Figure 5E). The small sampling areas of TMA rendered the majority of the samples not informative.

The spatial arrangement of VHL<sup>+</sup> and VHL<sup>-</sup> populations and their relationship to POSTN expression in clinical specimens recapitulated the findings in our preclinical metastatic ccRCC model (Figures 1C and 5B and Supplemental Figures 2A, 5F). These findings suggest that POSTN secreted by VHL<sup>-</sup> cells could be a key paracrine metastatic mediator in clinical disease.

### **VHL-KO cells and POSTN cause vascular destruction enhancing intravasation**

Detailed analysis of tumor-cell invasion into the circulation (i.e., circulatory tumor cells [CTCs]) in our metastatic preclinical model revealed that the presence of VHL-KO cells in mixed primary renal tumors enhanced the number of VHL-WT cells escaping into the circulation (Supplemental Figure 6A, 3C). These results suggested that VHL-KO cells could also exert an influence on vascular intravasation step of metastasis by disrupting the endothelial cell barrier as described in a recent study by Strilic and colleagues<sup>45</sup>. To examine the possible role of this mechanism in our tumor model, we established a 3D intravasation assay with a layer of either VHL-WT, VHL-KO, or a 1:1 mixture of the two placed above a layer of human umbilical vein endothelial cells (HUVEC), separated by a thin layer of Matrigel. After 48 hours, the integrity of the endothelial cell layer was tabulated, which showed significant endothelial cell destruction when cocultured with either VHL-KO or the 1:1 mixture but not with VHL-WT cells alone (Figure 6A). The molecular signals involved in the destruction of endothelial cells by the VHL-KO cells was further investigated. A wide range of tumor cell models are reported to induce necroptosis in endothelial cells, but RCC models have not been investigated<sup>45</sup>. Thus, we examined if our RC cells were able to induce either necroptosis or apoptosis in HUVEC endothelial cells. Coculturing with RC-VHL-WT or RC-VHL-KO cells did not activate the necroptosis markers MLKL or RIP in HUVECs (Figure 6B, C).

However, RC-VHL-KO cells induced a robust apoptotic response in endothelial cells, as indicated by cleaved caspase 3 (Figure 6B) and apoptosis reporter assays (Figure 6D). Importantly, the anti-POSTN blocking antibody blunted the HUVEC cell apoptosis induced by VHL-KO cells (Figures 6B and 6D). We further assessed endothelial destruction and vascular leakage in vivo in the CAM tumor system with the Miles assay. As shown in Figure 6E, the vasculature of the mixed tumors was leakier than that of the VHL-WT tumors.

In total, these results highlight that the POSTN protein secreted by VHL-KO cells could augment the escape of tumor cells into the blood circulation by destroying the endothelial cell barrier.

### **Inhibition of POSTN blocks metastasis in ccRCC models**

Given the multiple paracrine influences exerted by POSTN on the metastatic cascade, we assessed whether blocking POSTN with genetic and pharmacological approaches could suppress metastasis in vivo. The RC-VHL/POSTN-KO double-knockout cell line exhibited reduced promotion of VHL-WT cell motility in coculture (Figure 4G). Renal tumors containing 1:1 mixtures of VHL-WT cells and VHL/POSTN-KO cells showed reduced lung metastasis comparing mixed tumors with VHL-WT and VHL-KO cells, as measured by BLI (Figure 7A). We further determined if the anti-POSTN-blocking antibody could therapeutically inhibit the development of lung metastasis. As shown in Figures 7B-E, treatment with anti-POSTN antibody MPC5B4 greatly suppressed lung metastasis as assessed by gross lung morphology (Figure 7B), lung weight (Figure 7C), histological assessment by H&E (Figure 7D) and IF staining (Figure 7E). The POSTN blocking treatment did not impact primary tumor growth significantly (Figure 7F). We further assessed the anti-POSTN antibody treatment on the CAM PDX mixed tumor with 1:1 VHL+ and VHL-KO cells of case #22. Administration of MPC5B4 to the CAM PDX mixed tumors significantly reduced tumor cell dissemination into the chick embryo liver (Figure 7G and 7H) without significant reduction in primary tumor growth (Figure 7I). This finding fully recapitulated the therapeutic impact of MPC5B4 in the RC preclinical model.

This showed that POSTN is likely a critical paracrine factor secreted by VHL-KO cells that exerts multiple prometastatic influences, such as the EMT and motility in VHL-WT cells and the destruction of adjacent blood vessels (Figure 8A). Thus, targeted blockade of POSTN appears to be a promising approach to inhibit the deadly metastatic process in ccRCC.

Taken together, our VHL-deleted ccRCC models reveal a novel metastatic mechanism that relies on cooperative interactions between two distinct populations of tumor cells: VHL-KO (VHL<sup>-</sup>) and VHL-WT (VHL<sup>+</sup>) cells (Figure 8B). VHL-KO cells displayed an EMT and highly motile phenotype, but grow poorly in vivo. However, VHL-KO cells induced an aggressive behavior in VHL-WT cells that promoted rampant lung metastases composed predominantly of VHL-WT cells. Many of the phenotypes observed in our preclinical model were consistent in clinical tumor specimens, in particular, the loss of VHL resulted in the upregulation of POSTN. These results lend credibility to a cooperative mechanism of metastasis operating in human ccRCC. The discovery of the novel cooperative metastatic mechanism and the demonstration of the critical metastatic cross talk open up novel therapeutic avenues to control metastases in ccRCC.

## Discussion

In RCC and other epithelial cancers, metastasis is the major cause of mortality. The complex nature of metastasis coupled with an incomplete understanding of its mechanisms pose significant challenges to devising effective treatments. For the last three decades, the progression model has been the most common, prevailing concept for how metastasis occurs<sup>46</sup>. This model postulates that multiple progressive mutational events occur to enable a small fraction of cells to acquire full metastatic

potential. Subsequent studies showed that clonal evolution and selection can enhance not only metastatic potential but also achieve metastatic site specificity<sup>47,48</sup>. The cooperative model of metastasis uncovered here proposes a distinctly different mechanism in which signals between two populations of tumor cells, rather than clonal progression of a single population, is needed to achieve metastasis.

In the three metastatic ccRCC models reported here, the prerequisite prometastatic interactions occur between VHL-KO (VHL<sup>-</sup>) and VHL-WT (VHL<sup>+</sup>) cells. Intriguingly, EMT<sup>+</sup> VHL-KO cells are themselves poorly proliferative, but serve as the metastatic driver to induce aggressive behavior in the normally nonmetastatic VHL-WT cells. We further found that the loss of VHL function upregulates HIF1 $\alpha$ , which in turn stimulates the production of POSTN. POSTN serves as the critical, paracrine, metastasis-promoting factor by not only inducing EMT and motility in neighboring VHL-WT cells, but also causing vascular destruction to facilitate the escape of tumor cells into the circulation. Given that POSTN can impact the metastatic process in multiple ways, we showed that blocking POSTN's function can, indeed, halt lung metastasis in our models. The clinical relevance of the cooperative mechanism of metastasis is supported by the fact that human tumor samples consistently showed intratumoral heterogeneity with VHL<sup>-</sup> and VHL<sup>+</sup> tumor cell clusters in individual cases of ccRCC. We further demonstrated that POSTN overexpression is observed in VHL-nonexpressing areas of ccRCC tumors similar to our preclinical model.

The identification of the direct and instrumental role of POSTN in metastasis is a novel and significant finding. POSTN, also known as osteoblast-specific factor 2, is a ubiquitous, secreted, stromal protein that promotes integrin-dependent cell adhesion and motility during bone and cardiac development<sup>49,50</sup>.

POSTN overexpression is observed under EMT and hypoxic conditions<sup>50,51</sup>, the conditions of our VHL-KO cells. POSTN was reported to bridge the colonization of breast cancer cells to their terminal lung-metastatic site<sup>41</sup>, placing POSTN's involvement at the distal end of the metastatic cascade. This result differs from ours in that POSTN acts at the tumor-proximal intravasation step. We have not fully investigated POSTN's role in the latter steps of the metastatic cascade in our ccRCC models. An anti-POSTN neutralizing antibody has also been shown to be effective in blocking metastatic progression in an ovarian cancer model<sup>52</sup>. As such, the clinical applicability of a POSTN-targeted therapeutic approach to block metastasis clearly warrants further investigation.

The cooperative "team work" concept between distinct populations of tumor cells to advance the disease has also been reported in a recent study of breast cancer<sup>53</sup>. In this study, overexpression of EMT transcription factors that activate Hedgehog/GLI signaling promoted aggressive behavior in non-EMT cells in a paracrine manner. The cooperation between EMT and non-EMT cells reported is highly reminiscent of the crosstalk in our VHL-KO and VHL-WT model, but with POSTN as the functional mediator in our model. The cooperative, metastatic model proposed here and by others<sup>53</sup> emphasizes the need for different strategies to search for novel therapeutic targets.

Intratumoral heterogeneity in gene expression is widely recognized in ccRCC, and high-power gene sequencing technologies and bioinformatics have been applied to the study of this disease<sup>54,55</sup>. Despite these advances in the study of ccRCC, untangling the signaling pathways to distill the key cross talk signals remains very challenging. A potentially fruitful approach could be to first separate the distinct populations based on cellular morphology or protein biomarker(s) and then interrogate the expression in the distinct populations. Furthermore, in pathways such as VHL and HIFa that involve extensive post-transcriptional regulation of protein stability, it would be prudent to integrate protein expression with gene-expression analyses to gain a comprehensive view of the tumor biology. In sum, the study reported here provides an alternate idea of how the complex task of metastasis can be achieved by a heterogeneous tumor such as ccRCC. This cooperative model can guide the search for better and more effective treatments to block metastases and address a clearly unmet need in the field of cancer research.

## Methods And Materials

### Cells, plasmids, and reagents

The RENCA (RC) cell line was purchased from ATCC and was maintained in RPMI-1640 supplemented with 10% fetal bovine serum and 1X penicillin/streptomycin (Thermo Fisher, CA, USA, catalog number: 15140122). All CRISPR/Cas9-mediated knockout RC cell lines were selected with puromycin and clonally purified via single-cell cloning in a 96-well plate. A lentiviral vector encoding HA-tagged mStrawberry (modified from pSicoR, Addgene, MA, USA, catalog number: 11579) was used to label RC-VHL-WT cells, while a vector with the same backbone encoding flag-tagged EGFP was used to label RC-VHL-KO, RC-VHL/HIF1A-KO, and RC-VHL/POSTN-KO cells. In addition, for in vivo studies, all cell lines were also marked with lentivirus expressing firefly luciferase to permit BLI. pGL3-basic was from Promega (CA, USA, catalog number: E1751) and was enzymatically digested with MluI and XhoI. The periostin promoter was cloned from the genomic DNA of RC cells with the following primers: forward – CGACGCGTTAAGGTGGACAGTGAGGAAGACACA, reverse – CCGCTCGAGTTGAGAAGAACGAGAGTAGAGATTTTAGG. The control *renilla* luciferase vector was pRL-TK from Promega (CA, USA, catalog number: E2231). The plasmid for overexpressing constitutively-active *HIF1A* was from Addgene (MA, USA, catalog number: 44028).

### Time-lapse microscopy for 2D scratch assay and 3D migration assay

A total of  $1 \times 10^5$  tumor cells (e.g.,  $5 \times 10^4$  cells each of VHL-WT and VHL-KO cells) were grown on a 24-well plate until reaching 90% confluence. The bottom of each well was scratched with the end of a 200  $\mu$ l tip to form a gap. The cell migration was monitored continuously with a Nikon Eclipse Ti-E time-lapse microscope using a 10X objective, and a humidified, 37 °C environment containing 5% CO<sub>2</sub>. Specific fields of interest were set and recorded at 15 minutes intervals for 20 hours using the FITC and TRITC channels. Nikon elements software was used to measure the migration speed of cells in each group.

Transwell chambers (0.4  $\mu\text{m}$  pore size, Thermo Fisher, catalog number: CLS3470-48EA) were assembled in a 24-well plate. One milliliter of RPMI-1640 medium supplemented with 10% fetal bovine serum and 50 ng/mL EGF was added to the bottom chamber. HUVECs were seeded on the bottom of the Transwell chamber at a cell number of  $1 \times 10^5$ . On day 2, a layer of Matrigel (Corning, catalog number: 356234) was coated on top of the layer of HUVECs and placed back in a 37 °C incubator to solidify: 100  $\mu\text{L}$  for migration assay or 30  $\mu\text{L}$  for 3D in vitro intravasation assay. Tumor cells ( $1 \times 10^5$ ) were then seeded onto the top of the Matrigel. A Nikon Eclipse Ti-E time-lapse confocal microscope was used to image cell migration. The z-step parameters were set with the HUVEC cell layer as the bottom and the tumor cell layer as the top with approximately 200 stepwise stacks for scanning every 15 minutes for 48 hours.

### **Western blot, necroptosis, and apoptosis reporter assay**

For Western blot,  $1 \times 10^6$  HUVECs were seeded onto the bottom of 6-well-plate Transwell chambers (1  $\mu\text{m}$  pore size, Falcon, catalog number: 353102) with  $1 \times 10^6$  tumor cells in the top chamber, with or without 1  $\mu\text{g}/\text{mL}$  anti-POSTN MPC5B4 monoclonal antibody (mAb), with or without cilengitide in concentrations indicated in the figure legends. Cells were harvested after 48 hours for whole-cell-lysate protein extraction with RIPA buffer (ThermoFisher, catalog number: 89901) supplemented with proteinase inhibitors (Thermo Fisher, catalog number: 78430). Samples were then boiled for 10 minutes in 6X SDS loading buffer and loaded onto the 10% gels. Blots were probed with anti-phospho-RIP (Ser166)(1:1000), anti-RIP(1:1000), anti-phospho-MLKL (Ser358)(1:1000), anti-MLKL(1:1000), anti-caspase-3(1:1000), and anti-cleaved caspase-3(1:1000) from the Apoptosis/Necroptosis Antibody Sampler Kit (Cell Signaling Technology, MA, USA, catalog number: 92570). Blots were imaged and analyzed on a ChemiDoc XRS+ with associated Image Lab software (Bio-Rad).

For the necroptosis reporter assay, 24-well-plate Transwell chambers (0.4  $\mu\text{m}$  pore size, Thermo Fisher, CA, USA, catalog number: CLS3470-48EA) were seeded with  $1 \times 10^5$  HUVECs on the bottom and  $1 \times 10^5$  tumor cells on the top of the chamber with or without 1  $\mu\text{g}/\text{mL}$  anti-POSTN MPC5B4 mAb. After 48 hours, HUVECs were washed with PBS once and a solution of 1.6  $\mu\text{M}$  ethidium homodimer III (EthD-III, Biotium, CA, USA, catalog number: 400050) and 2  $\mu\text{M}$  Hoechst33342 (Biotium, CA, USA, catalog number: 40045) were added to cells and incubated in a humidified, 5%  $\text{CO}_2$  incubator at 37 °C for 15 minutes. Microscope images were taken of five random fields of each well with a 10X objective in DAPI and TRITC channels and quantified with ImageJ.

For apoptosis evaluation, HUVECs were cultured in Transwell chambers as described above. After 48 hours, the plates were equilibrated at room temperature for 10 minutes, and 200  $\mu\text{L}$  of Caspase-Glo 3/7 reagent (Promega, catalog number: G8090) was added to each well. After being placed on a shaker at 300-500 RPM for 30 seconds, the reaction was incubated at room temperature for 1 hour and then analyzed for luminescence with a Synergy HT microplate reader (BioTek).

### **Cell proliferation assay**

Cell proliferation was measured using the MTS assay and direct cell counting. For both assays, cells in log phase were counted and seeded on day 0 at a density of 1000 cells per well onto a 96-well plate, or 500 cells per well onto a 384-well plate. For the MTS assay, cell numbers were evaluated every 24 hours on days 1, 2, 3, 4, 5, and 6 using the MTS kit (Promega, CA, USA, catalog number: G3582) and measured with a Multiskan MK3 microplate reader (Thermo, USA). For direct cell counting, an ImageXpress workstation was used to photograph each well of a 384-well plate and count the DAPI-stained cells.

### **CAM tumor xenograft model, renal tumor implantation, and anti-periostin treatment studies in mice.**

Establishment of CAM tumor xenografts and their analyses were performed as previously described<sup>34,56,57</sup>. Intrarenal implantation of  $1 \times 10^6$  total RC or AC tumor cells was performed as previously described<sup>29,36</sup>. One week after implanting a 1:1 mixture of VHL-WT to VHL-KO cells, 10 mg/kg of MPC5B4 mAb was injected via tail vein three times per week for 4 weeks. The animals were imaged and sacrificed. Tissues were harvested, fixed, paraffin embedded, and cut for histological analyses.

### **IHC and IF staining**

Slides were baked at 65 °C for 20 minutes and deparaffinized through three 10min incubations in xylene then rehydrated in stepwise dilutions of ethanol from 100% to 50% followed by water. Citrate buffer was used for antigen retrieval in a vegetable steamer for 25 minutes. Blocking used 1% BSA, and the following primary antibodies were incubated overnight at 4 °C: anti-VHL (1:200, Abcam, USA, catalog number: ab135576), anti-flag (1:200, eBioscience, USA, catalog number: 14-6681-82), anti-HA (1:200, Santa Cruz Biotechnology, USA, catalog number: sc805), and anti-Ki67 (1:200, Vector Laboratories, USA, catalog number: VP-RM04). After three 7-minute washes in TBST, slides were incubated with secondary antibody (goat-anti-rabbit, catalog number: 111-035-045; goat-anti-mouse, catalog number: 115-035-062; both from Jackson ImmunoResearch Laboratories, USA) at a 1:200 dilution. Slides were washed three times in TBST for 7 minutes each. For IHC, slides were incubated with DAB (Biocare Medical, USA, catalog number: DB801R) and counterstained with hematoxylin. For IF, slides were incubated with FITC-conjugated TSA (Perkin Elmer, USA, catalog number: SAT701001EA) or CY3-conjugated TSA (Perkin Elmer, USA, catalog number: NEL744001KT). After TSA staining, Hoechst 33342 was added to the slides for nuclear staining, and slides were sealed with glycerol then scanned at UCLA's Translational Pathology Core Laboratory (UCLA).

In addition, spatial quantification analyses for slide case #22 were performed using HALO™ Image Analysis program by Indica Labs (USA). An initial positive stain tissue marker analysis was conducted with proper nuclear segmentation and dye threshold intensities. Under HALO™ 3.0 Spatial Analysis Module, infiltration and density heat map algorithms were used to establish spatial relationships important for VHL-POSTN paracrine crosstalk.

### **Flow cytometry**

Primary tumors and lungs of mice were dissected, minced into small pieces, and digested with 0.2% collagenous II at 37 °C on a 100 RPM shaker. The cell suspensions were passed through 70-µm cell strainers. The digested cells were stained with Hoechst 33342 for 15 minutes and analyzed by flow cytometry. Similarly, chicken and mouse blood were collected and lysed with red blood cell lysis buffer (BD Bioscience, USA, catalog number: 555899). Cells were then analyzed by flow cytometry for mStrawberry and EGFP expression.

### **Isolation and cultivation of primary ccRCC tumor cells.**

With the consent of patients, primary ccRCC tumor samples were collected and chopped into pieces with sterile scissors and scalpels into RPMI-1640. Tissue chunks were transferred to a 15-mL conical tube and centrifuged at 300 x g at room temperature for 5 minutes. The supernatants were carefully discarded and the tissue pellet was resuspended in 2.6-mL prediluted 3 U/L Liberase TM (Sigma-Aldrich, catalog number: 5401119001) in RPMI-1640 media. The tube was placed on a 100 RPM rotator at 37 °C for 1 hour. When the tissue was fully digested and no chunks were visible, cells were centrifuged at 300 x g at room temperature for 5 minutes. The pellet was further treated with prediluted 1X red blood cell lysis buffer (BD Biosciences, catalog number: 555899) in sterile water for 15 minutes and washed once with PBS. Cells were resuspended in RPMI-1640 supplemented with 10% fetal bovine serum and 1X penicillin/streptomycin and cultured in a humidified, 5% CO<sub>2</sub> incubator at 37 °C.

### **Human ccRCC patient specimens**

The tissue microarray was constructed from a cohort of 357 patients who underwent nephrectomy for sporadic RCC at UCLA between 1989 and 2000, as previously described<sup>44</sup>. Clinical data, including age, gender, Eastern Cooperative Oncology Group performance status, and pathologic data (including tumor-node-metastasis stage, histologic subtype, and Fuhrman grade) were collected for each case. This study was approved by the UCLA Institutional Review Board.

Large tumor tissues from primary tumors, locally invasive tumors, or metastases were obtained from 26 patients who underwent radical nephrectomy in the Department of Urology at the Ronald Regan Medical Center, UCLA, from 2015 to 2018. All patients provided informed consent before surgery, and all experiments were performed according to the approved guidelines, complying with the principles for the use of human tissues under the Declaration of Helsinki. This study was approved by the Institutional Review Board of UCLA, IRB Protocol #11-001363.

### **Whole exome sequencing and data analysis from TCGA-KIRC database**

Genomic DNA from 4 pieces of tumor chunks from patient #22 and the patient derived cell line were extracted and run whole exome sequencing (WES) at The Technology Center for Genomics & Bioinformatics (TCGB). Subsequently, WES data was aligned to human genome GRCh37 and processed following GATK v4.1.4.0 best practices<sup>58</sup>. Mutation calls were made using Mutect2<sup>59</sup> and known variants were annotated using VEP<sup>60</sup>. Copy number calls were made using CNVkit v0.9.1<sup>61</sup> with tumor

samples matched to a neutral copy number in silico reference genome. Copy number events were mapped to the gene-level using the R package CNTools v1.38.0<sup>62</sup>. Without sequenced normal samples to filter out germline SNPs, variant calls were filtered using COSMIC by only selecting mutations that were present in the database. For comparisons between matched samples, variants were further filtered to those with VEP impact rating above “LOW” and variant allele frequency (VAF) greater than 0.1.

While for the TCGA-KIRC dataset, Mutect2 MAF variant allele frequencies and SEG file copy number data for TCGA-KIRC samples were accessed through the Genomics Data Commons<sup>63</sup>. Consensus estimates of tumor purity combining available measures from WES (ABSOLUTE), methylation profiling (LUMP), RNA sequencing (ESTIMATE), and IHC analysis were collected from the study of Aran D et al<sup>64</sup> and estimates of tumor ploidy based on ABSOLUTE from that of Hoadley KA et al<sup>65</sup>. Samples were filtered for those where complete data was available and purity estimate greater than 0.4. Samples were also further filtered for those with reasonable agreement between ABSOLUTE and ESTIMATE purity estimates (difference less than 0.3), resulting in the removal of 21 samples. For VAF adjustment, adjusted frequencies between 1 and 1.1 were set to 1. Three samples with incompatible values within our equations was removed from analysis. Supplemental analysis using only ABSOLUTE estimates of tumor purity further reduced sample sizes since not all samples with consensus estimates of purity had contributing ABSOLUTE estimates and ABSOLUTE estimates more often (n = 17) led to incompatible values in our equations. Copy number and allele frequencies were adjusted to account for tumor purity and ploidy by assuming that the normal contamination is diploid, and using the following formulas:

$$CN_t = \frac{2^{CNR} * (2 * (1 - PT_t) + PL_t * PT_t) - 2 * (1 - PT_t)}{PT_t}$$

$$CNR_{adj} = \log_2\left(\frac{CN_t}{2}\right)$$

$$AF_{adj} = \frac{VAF * (PT_t * CN_t + (1 - PT_t) * 2)}{PT_t * CN_t}$$

$CN_t$  = Tumor copy number

$PT_t$  = Tumor purity

$PL_t$  = Tumor ploidy

CNR = Observed log2 copy number ratio

$CNR_{adj}$  = Purity and ploidy adjusted copy number ratio

$AF_{adj}$  = Purity and ploidy adjusted somatic variant allele frequency

VAF = Observed variant allele frequency

## Single cell sequencing and analysis

Single cells were prepared for single cell RNA sequencing by Liberase (Cat#5401119001, Sigma Aldrich, USA) at 13u/ml mediated digestion of the tissue from the patient and filtered through 70um cell strainer. RNA extraction and sequencing were performed by the Technology Center for Genomics & Bioinformatics (TCGB) at UCLA on the Illumina NextSeq500 platform with single-end 1x75 base pair read length. Single cell RNA sequencing results were demultiplexed and aligned to the prebuilt human reference genome GRCh38-2020-A annotated with transcript information from GENCODE v32 using the Cell Ranger v4.0.0 pipeline following all default parameters to generate count matrices<sup>66</sup>. Single cell data was filtered to include cells with total counts greater than 2,000, total number of expressed genes greater than 1,000, and percentage of mitochondrial reads less than twenty percent. Unnormalized raw count data was input to scImpute v0.0.9 for identification of read dropout events and imputation<sup>67</sup>. Count matrices were then processed using the Seurat v4 workflow for data transformation and scaling, dimensionality reduction through uniform manifold approximation and projection (UMAP), and differential expression through the MAST package<sup>68-70</sup>. Geneset enrichment analysis (GSEA) was then carried out using FGSEA v1.14.0 on a gene list pre-ranked with signed log<sub>10</sub> p-values from the differential expression results<sup>71</sup>. Genesets from the Hallmarks, KEGG, and Reactome databases accessed through the msigdb v7.1.1 package were included in analyses<sup>72</sup>.

## Bulk RNA sequencing and analysis

RENCA and ACHN cells for bulk RNA sequencing were trypsinized and sent to the TCGB at UCLA for subsequent sample processing including RNA extraction and DNase treatment. Libraries were sequenced on the Illumina HiSeq3000 platform with single-end 1x50 base pair read length. Gene expression quantification from bulk RNA sequencing was generated using Salmon v1.2.1 run in mapping-based mode<sup>73</sup>. Reads were selectively aligned to the GENCODE vM25 mouse reference transcriptome with corrections for sequence-specific and GC content biases. Gene count data were then processed using the DESeq2 v1.22.2 package for normalization and differential expression analysis<sup>74</sup>. As with single cell data, GSEA was carried out using FGSEA v1.14.0 on pre-ranked gene lists. For RENCA models the signed log<sub>10</sub> p-value was used for gene list ranking and for ACHN models the log<sub>2</sub> fold change of gene CPMs were used where no p-value could be calculated.

## Identification of preserved gene expression signatures across RNA sequencing datasets

Concordant changes in gene expression between VHL+ vs. VHL- cells in single cell RNA sequencing, VHL+ vs. VHL- ACHN models, and VHL+ vs. VHL- RENCA models were identified by calculating the signal-to-noise ratio (squared mean divided by the sample variance) of log<sub>2</sub> fold changes across the three comparisons for each gene. The top 200 genes based on this metric were then selected for clustering using Ward's minimum variance method and plotting using the heatmap v1.0.12 package<sup>75</sup>. A similar

approach was then applied to the NES scores from the GSEA results from each comparison and the top 30 genesets based on this metric were selected.

## **Statistics**

Each experiment was performed at least in triplicate unless otherwise stated. Data are presented as mean  $\pm$  standard deviation (SD). Significance was determined by a paired, Student's t-test when there were two groups or by a one-way ANOVA when there were three or more groups (GraphPad Prism version 6.0). A p-value cutoff of 0.05 was used to establish significance.

## **Declarations**

### **ACKNOWLEDGEMENTS**

This study was supported by the NCI/NIH (grant number 1R21CA216770), Tobacco-Related Disease Research Program (grant number 271R-0016), CDMRP Kidney Cancer Research Program (grant number W81XWH-20-1-0918) and Cancer Research Coordinating Committee (grant number CRC15-380768) to L.W. UCLA institutional support grants included the UCLA Jonsson Comprehensive Cancer Center (grant number P30CA016042) and the UCLA Clinical and Translational Science Institute (grant number UL1TR001881) to L.W. We deeply appreciate Professor Desmond Smith's critical review of our manuscript. We thank the UCLA Translational Pathology Core Laboratory for preparing tumor samples, especially Dr. Yunfeng Li for her timely and meticulous help. Also, we appreciate the professional microscopy assistance of the Nikon Microscopy team members, including TJ Kelly, Ramunas Stanciauskas, Andrew Brumm, and Patrick Keenan.

### **AUTHOR CONTRIBUTIONS**

Conceptualization: Ju. H., S. S., and L.W.; methodology: Ju.H. and S.S.; investigation: Ju. H., P.T., M. I., N. A. B., Z. T., W. G., L. Y., R. Z., J. G. R., P. S. J., R. M. P., J. S., and T. G. G.; resources: P. S. J., J. V. S., Ji. H., A.P., A. I. C., and H. X.; project administration: L.W.; writing original draft: Ju. H. and L.W.; writing, review, and editing: B. S. K., A. I. C., S. S., and L. W.; funding H.X. and L.W.; supervision: L.W.

### **COMPETING INTERESTS**

The University of California, Los Angeles has a pending patent application USP P-581130 (Ju. H., S.S., and L.W.) relevant to this study.

## References

1. Jemal, A., et al. Global cancer statistics. *CA: a cancer journal for clinicians* 61, 69-90 (2011).
2. Bianchi, M., et al. Distribution of metastatic sites in renal cell carcinoma: a population-based analysis. *Annals of oncology : official journal of the European Society for Medical Oncology* 23, 973-980 (2012).
3. Rini, B.I., et al. Pembrolizumab plus Axitinib versus Sunitinib for Advanced Renal-Cell Carcinoma. *The New England journal of medicine* 380, 1116-1127 (2019).
4. Latif, F., et al. Identification of the von Hippel-Lindau disease tumor suppressor gene. *Science* 260, 1317-1320 (1993).
5. Maher, E.R., Yates, J.R. & Ferguson-Smith, M.A. Statistical analysis of the two stage mutation model in von Hippel-Lindau disease, and in sporadic cerebellar haemangioblastoma and renal cell carcinoma. *Journal of medical genetics* 27, 311-314 (1990).
6. Foster, K., et al. Foster K, Prowse A, van den Berg A, Fleming S, Hulsbeek MM, Crossey PA, Richards FM, Cairns P, Affara NA, Ferguson-Smith MA, Buys CHM, Maher ER Somatic mutations of the von Hippel-Lindau disease tumour suppressor gene in non-familial clear cell renal carcinoma. *Hum Mol Genet* 3: 2169-2173, (1994).
7. Whaley, J.M., et al. Germ-line mutations in the von Hippel-Lindau tumor-suppressor gene are similar to somatic von Hippel-Lindau aberrations in sporadic renal cell carcinoma. *American journal of human genetics* 55, 1092-1102 (1994).
8. Young, A.C., et al. Analysis of VHL Gene Alterations and their Relationship to Clinical Parameters in Sporadic Conventional Renal Cell Carcinoma. *Clinical cancer research : an official journal of the American Association for Cancer Research* 15, 7582-7592 (2009).
9. Gossage, L., Eisen, T. & Maher, E.R. VHL, the story of a tumour suppressor gene. *Nature reviews. Cancer* 15, 55-64 (2015).
10. Sato, Y., et al. Integrated molecular analysis of clear-cell renal cell carcinoma. *Nature genetics* 45, 860-867 (2013).
11. Ivan, M., et al. HIF $\alpha$  targeted for VHL-mediated destruction by proline hydroxylation: implications for O<sub>2</sub> sensing. *Science* 292, 464-468 (2001).
12. Jaakkola, P., et al. Targeting of HIF- $\alpha$  to the von Hippel-Lindau ubiquitylation complex by O<sub>2</sub>-regulated prolyl hydroxylation. *Science* 292, 468-472 (2001).

13. Semenza, G.L. Hypoxia-inducible factors: mediators of cancer progression and targets for cancer therapy. *Trends in pharmacological sciences* 33, 207-214 (2012).
14. Bajorin, D.F., Motzer, R.J. & Bosl, G.J. Advances in Urologic Oncology: Results Progress From Successful Interdisciplinary Research. *Journal of Clinical Oncology* 24, 5479-5481 (2006).
15. Mandriota, S.J., et al. HIF activation identifies early lesions in VHL kidneys: evidence for site-specific tumor suppressor function in the nephron. *Cancer cell* 1, 459-468 (2002).
16. Rankin, E.B., Tomaszewski, J.E. & Haase, V.H. Renal Cyst Development in Mice with Conditional Inactivation of the von Hippel-Lindau Tumor Suppressor. *Cancer Research* 66, 2576 (2006).
17. Frew, I.J., et al. pVHL and PTEN tumour suppressor proteins cooperatively suppress kidney cyst formation. *The EMBO journal* 27, 1747-1757 (2008).
18. Hsu, T. Complex cellular functions of the von Hippel-Lindau tumor suppressor gene: insights from model organisms. *Oncogene* 31, 2247-2257 (2012).
19. Albers, J., et al. Combined mutation of Vhl and Trp53 causes renal cysts and tumours in mice. *EMBO molecular medicine* 5, 949-964 (2013).
20. Hu, C.-J., Wang, L.-Y., Chodosh, L.A., Keith, B. & Simon, M.C. Differential Roles of Hypoxia-Inducible Factor 1 $\alpha$  (HIF-1 $\alpha$ ) and HIF-2 $\alpha$  in Hypoxic Gene Regulation. *Molecular and Cellular Biology* 23, 9361-9374 (2003).
21. Raval, R.R., et al. Contrasting properties of hypoxia-inducible factor 1 (HIF-1) and HIF-2 in von Hippel-Lindau-associated renal cell carcinoma. *Mol Cell Biol* 25, 5675-5686 (2005).
22. Shen, C., et al. Genetic and Functional Studies Implicate HIF1 $\alpha$  as a 14q Kidney Cancer Suppressor Gene. *Cancer Discovery* 1, 222-235 (2011).
23. Fu, L., Wang, G., Shevchuk, M.M., Nanus, D.M. & Gudas, L.J. Generation of a Mouse Model of Von Hippel-Lindau Kidney Disease Leading to Renal Cancers by Expression of a Constitutively Active Mutant of HIF1 $\alpha$ . *Cancer Research* 71, 6848-6856 (2011).
24. Fu, L., Wang, G., Shevchuk, M.M., Nanus, D.M. & Gudas, L.J. Activation of HIF2 $\alpha$  in kidney proximal tubule cells causes abnormal glycogen deposition but not tumorigenesis. *Cancer research* 73, 2916-2925 (2013).
25. Keith, B., Johnson, R.S. & Simon, M.C. HIF1 $\alpha$  and HIF2 $\alpha$ : sibling rivalry in hypoxic tumour growth and progression. *Nature reviews. Cancer* 12, 9-22 (2011).
26. Cowey, C.L. & Rathmell, W.K. VHL gene mutations in renal cell carcinoma: role as a biomarker of disease outcome and drug efficacy. *Current oncology reports* 11, 94-101 (2009).

27. Thomas, G.V., et al. Hypoxia-inducible factor determines sensitivity to inhibitors of mTOR in kidney cancer. *Nature Medicine* 12, 122 (2005).
28. Pantuck, A.J., An, J., Liu, H. & Rettig, M.B. NF- $\kappa$ B-Dependent Plasticity of the Epithelial to Mesenchymal Transition Induced by *Von Hippel-Lindau* Inactivation in Renal Cell Carcinomas. *Cancer Research* 70, 752-761 (2010).
29. Schokrpur, S., et al. CRISPR-Mediated VHL Knockout Generates an Improved Model for Metastatic Renal Cell Carcinoma. *Scientific reports* 6, 29032 (2016).
30. Thiery, J.P. Epithelial-mesenchymal transitions in tumour progression. *Nature reviews. Cancer* 2, 442-454 (2002).
31. Kalluri, R. & Weinberg, R.A. The basics of epithelial-mesenchymal transition. *The Journal of clinical investigation* 119, 1420-1428 (2009).
32. Fischer, K.R., et al. Epithelial-to-mesenchymal transition is not required for lung metastasis but contributes to chemoresistance. *Nature* 527, 472-476 (2015).
33. Zheng, X., et al. Epithelial-to-mesenchymal transition is dispensable for metastasis but induces chemoresistance in pancreatic cancer. *Nature* 527, 525-530 (2015).
34. Hu, J., Ishihara, M., Chin, A.I. & Wu, L. Establishment of xenografts of urological cancers on chicken chorioallantoic membrane (CAM) to study metastasis. *Precis Clin Med* 2, 140-151 (2019).
35. Creighton, C.J., et al. Comprehensive molecular characterization of clear cell renal cell carcinoma. *Nature* 499, 43-49 (2013).
36. Hu, J., et al. A Non-integrating Lentiviral Approach Overcomes Cas9-Induced Immune Rejection to Establish an Immunocompetent Metastatic Renal Cancer Model. *Molecular Therapy - Methods & Clinical Development* 9, 203-210 (2018).
37. Ribatti, D. The chick embryo chorioallantoic membrane as a model for tumor biology. *Experimental cell research* 328, 314-324 (2014).
38. Hagedorn, M., et al. Accessing key steps of human tumor progression *in vivo* by using an avian embryo model. *Proceedings of the National Academy of Sciences of the United States of America* 102, 1643-1648 (2005).
39. Giard, D.J., et al. In Vitro Cultivation of Human Tumors: Establishment of Cell Lines Derived From a Series of Solid Tumors<sup>2</sup>. *JNCI: Journal of the National Cancer Institute* 51, 1417-1423 (1973).
40. Michaylira, C.Z., et al. Periostin, a Cell Adhesion Molecule, Facilitates Invasion in the Tumor Microenvironment and Annotates a Novel Tumor-Invasive Signature in Esophageal Cancer. *Cancer*

Research 70, 5281-5292 (2010).

41. Malanchi, I., et al. Interactions between cancer stem cells and their niche govern metastatic colonization. *Nature* 481, 85-89 (2011).
42. Dahinden, C., et al. Mining Tissue Microarray Data to Uncover Combinations of Biomarker Expression Patterns that Improve Intermediate Staging and Grading of Clear Cell Renal Cell Cancer. *Clinical Cancer Research* 16, 88-98 (2010).
43. Field, S., et al. Novel highly specific anti-periostin antibodies uncover the functional importance of the fascilin 1-1 domain and highlight preferential expression of periostin in aggressive breast cancer. *138*, 1959-1970 (2016).
44. Klatte, T., et al. Hypoxia-inducible factor 1 alpha in clear cell renal cell carcinoma. *Clinical cancer research : an official journal of the American Association for Cancer Research* 13, 7388-7393 (2007).
45. Strilic, B., et al. Tumour-cell-induced endothelial cell necroptosis via death receptor 6 promotes metastasis. *Nature* 536, 215-218 (2016).
46. Nowell, P.C. The clonal evolution of tumor cell populations. *Science (New York, N.Y.)* 194, 23-28 (1976).
47. Kang, Y., et al. A multigenic program mediating breast cancer metastasis to bone. *Cancer cell* 3, 537-549 (2003).
48. Minn, A.J., et al. Genes that mediate breast cancer metastasis to lung. *Nature* 436, 518-524 (2005).
49. Takeshita, S., Kikuno, R., Tezuka, K. & Amann, E. Osteoblast-specific factor 2: cloning of a putative bone adhesion protein with homology with the insect protein fasciclin I. *The Biochemical journal* 294 ( Pt 1), 271-278 (1993).
50. Morra, L. & Moch, H. Periostin expression and epithelial-mesenchymal transition in cancer: a review and an update. *Virchows Archiv : an international journal of pathology* 459, 465-475 (2011).
51. Nakazawa, Y., et al. Periostin blockade overcomes chemoresistance via restricting the expansion of mesenchymal tumor subpopulations in breast cancer. *Scientific reports* 8, 4013-4013 (2018).
52. Zhu, M., et al. Neutralizing monoclonal antibody to periostin inhibits ovarian tumor growth and metastasis. *Molecular cancer therapeutics* 10, 1500-1508 (2011).
53. Neelakantan, D., et al. EMT cells increase breast cancer metastasis via paracrine GLI activation in neighbouring tumour cells. *Nature communications* 8, 15773 (2017).
54. Gerlinger, M., et al. Intratumor Heterogeneity and Branched Evolution Revealed by Multiregion Sequencing. *New England Journal of Medicine* 366, 883-892 (2012).

55. Turajlic, S., et al. Tracking Cancer Evolution Reveals Constrained Routes to Metastases: TRACERx Renal. *Cell* 173, 581-594.e512 (2018).
56. Ishihara, M., et al. Comparing Metastatic Clear Cell Renal Cell Carcinoma Model Established in Mouse Kidney and on Chicken Chorioallantoic Membrane. *JoVE*, e60314 (2020).
57. Sharrow, A.C., Ishihara, M., Hu, J., Kim, I.H. & Wu, L. Using the Chicken Chorioallantoic Membrane In Vivo Model to Study Gynecological and Urological Cancers. *JoVE*, e60651 (2020).
58. DePristo, M.A., et al. A framework for variation discovery and genotyping using next-generation DNA sequencing data. *Nature genetics* 43, 491-498 (2011).
59. Cibulskis, K., et al. Sensitive detection of somatic point mutations in impure and heterogeneous cancer samples. *Nature biotechnology* 31, 213-219 (2013).
60. McLaren, W., et al. The Ensembl Variant Effect Predictor. *Genome biology* 17, 122 (2016).
61. Talevich, E., Shain, A.H., Botton, T. & Bastian, B.C. CNVkit: Genome-Wide Copy Number Detection and Visualization from Targeted DNA Sequencing. *PLoS Comput Biol* 12, e1004873 (2016).
62. Zhang, J. CNTools: Convert segment data into a region by sample matrix to allow for other high level computational analyses. R package (Version 1.38.0) (2016).
63. Comprehensive molecular characterization of clear cell renal cell carcinoma. *Nature* 499, 43-49 (2013).
64. Aran, D., Sirota, M. & Butte, A.J. Systematic pan-cancer analysis of tumour purity. *Nature communications* 6, 8971 (2015).
65. Hoadley, K.A., et al. Multiplatform analysis of 12 cancer types reveals molecular classification within and across tissues of origin. *Cell* 158, 929-944 (2014).
66. Zheng, G.X., et al. Massively parallel digital transcriptional profiling of single cells. *8*, 14049 (2017).
67. Li, W.V. & Li, J.J. An accurate and robust imputation method scImpute for single-cell RNA-seq data. *Nature communications* 9, 997 (2018).
68. Hao, Y., et al. Integrated analysis of multimodal single-cell data. *Cell* 184, 3573-3587.e3529 (2021).
69. Leland McInnes, J.H., James Melville. UMAP: Uniform Manifold Approximation and Projection for Dimension Reduction. arXiv preprint arXiv 1802.03426(2018).
70. Finak, G., et al. MAST: a flexible statistical framework for assessing transcriptional changes and characterizing heterogeneity in single-cell RNA sequencing data. *Genome biology* 16, 278 (2015).

71. Korotkevich, G., Vladimir Sukhov, Nikolay Budin, Boris Shpak, Maxim N. Artyomov, and Alexey Sergushichev. Fast gene set enrichment analysis. *BioRxiv* 060012(2021).
72. Dolgalev, I. msigdb: MSigDB gene sets for multiple organisms in a tidy data format. (2019).
73. Patro, R., Duggal, G., Love, M.I., Irizarry, R.A. & Kingsford, C. Salmon provides fast and bias-aware quantification of transcript expression. *Nature Methods* 14, 417-419 (2017).
74. Love, M.I., Huber, W. & Anders, S. Moderated estimation of fold change and dispersion for RNA-seq data with DESeq2. *Genome biology* 15, 550 (2014).
75. Kolde, R., (Maintainer) Raivo Kolde. Package 'pheatmap'. *R package* 1 no. 7(2015).

## Figures

Figure 1

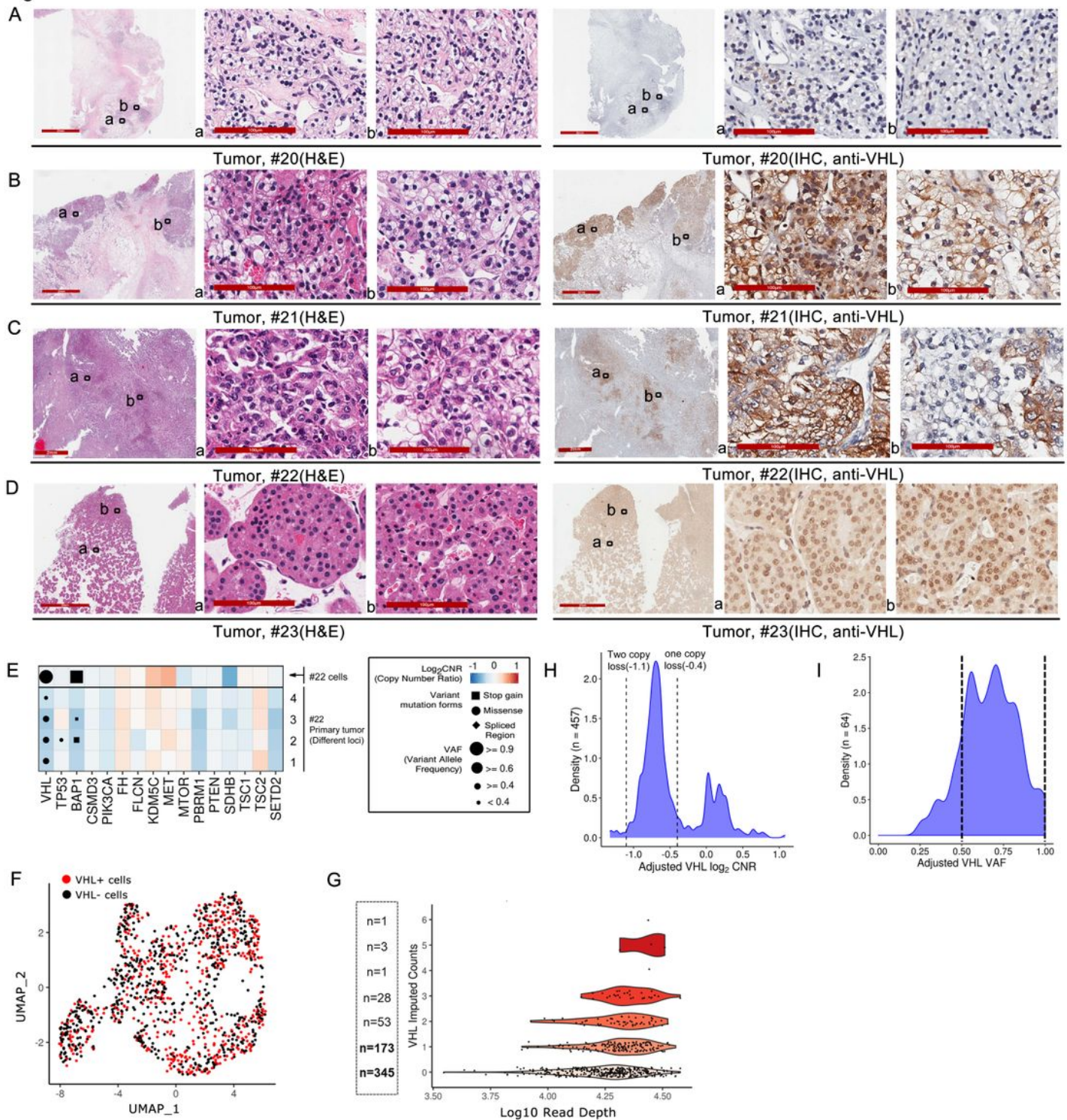


Figure 1

Human ccRCC tumor specimen showed intratumoral heterogeneity in VHL expression. H&E stain and VHL IHC performed on parallel sections of tumor from different cases of human RCC are shown in A) case #20, B) case #21, C) case #22 and D) case #23. E) Mutational data from WES of common oncogenic driver genes in ccRCC are shown for four loci of the patient's tumor and the derivative cell line of case #22. Point sizes represent variant allele frequencies. Values above 0.4 represent likely clonal mutations

and above 0.9 represent clonal mutations combined with loss of heterozygosity. Colors represent  $\log_2$  CNRs for each gene, with DNA gains in red and losses in blue. F) UMAP dimensionality reduction plot of single cell sequencing from the case #22 colored by VHL expression positivity in each cell. G) Scatterplot of sequencing depth vs. VHL imputed gene expression across non-cycling single cells from single cell sequencing in the case #22 with the number of cells at each expression level of VHL listed. H) Density plot showing the CNRs of the VHL locus in the TCGA-KIRC cohort (n = 459) after adjusting for both tumor purity and ploidy with consensus estimates of purity. A CNR value of -1.1 represents a two-copy loss of VHL (dotted line) and -0.4 indicates one copy loss. I) Density plot showing the VAF of somatic VHL mutations in the TCGA-KIRC cohort (n = 148) after adjusting for both tumor purity and ploidy (with consensus estimates of tumor purity).

Figure 2

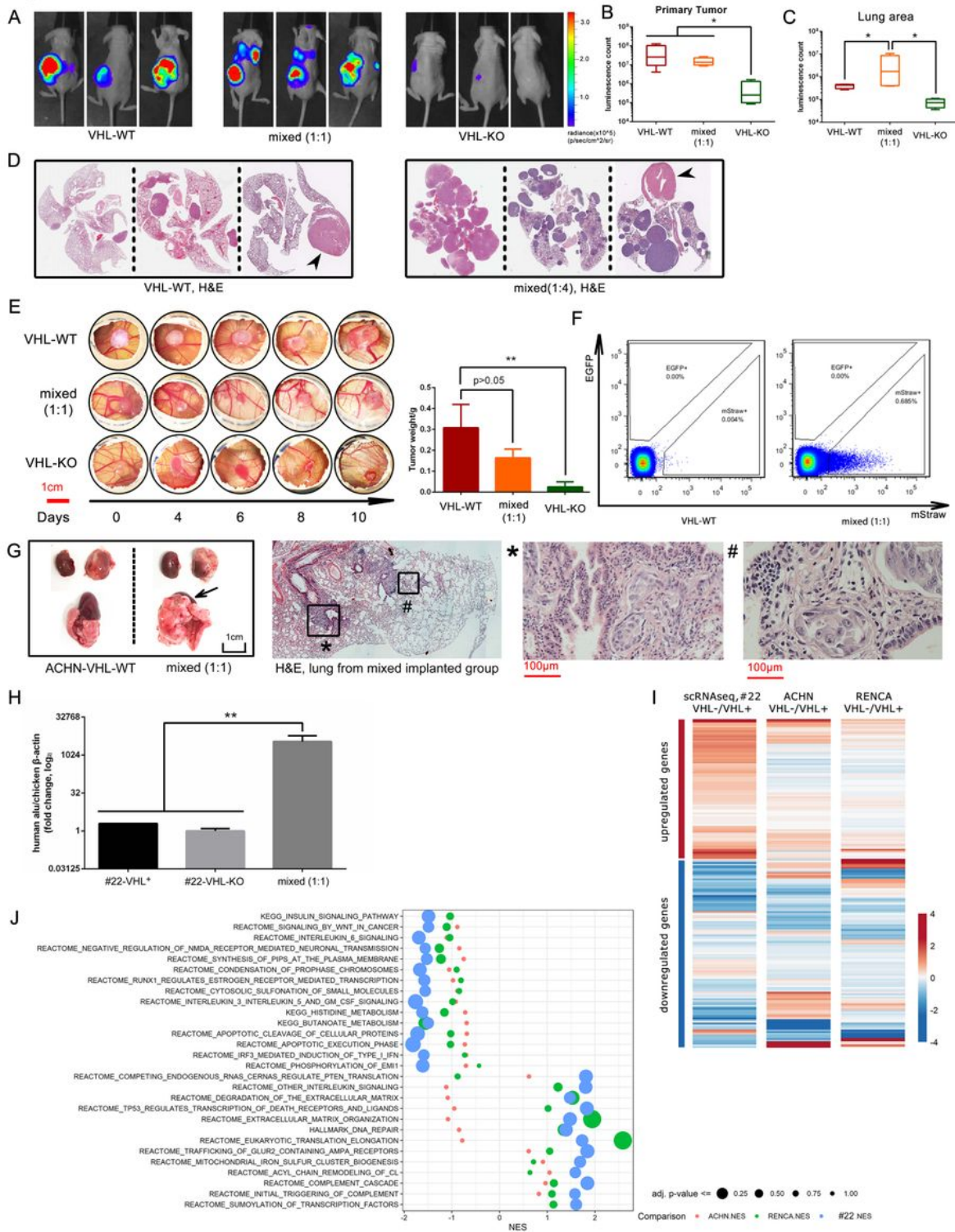


Figure 2

VHL-KO cells cooperate with VHL-WT cells to cause metastasis. A) Mice were implanted with a total of  $1 \times 10^6$  tumor cells, either RC-VHL-WT, RC-VHL-KO, or a 1:1 mixture of the two cell types, into their left kidney ( $n = 6$  per group). Images of three representative animals assessed by BLI on week 4 post implantation are shown. B) Primary tumor indicated by BLI in different groups are shown at the end point. C) Lung metastasis are indicated by elevated BLI signals in the thoracic cavity in the mixed tumor group.

D) H&E-stained sections (low magnification) of lung and heart in the RC-VHL-WT tumor group and mixed (1:4) tumor group. Arrowhead indicates the heart. E) RC tumor growth was assessed in the CAM tumor system through longitudinal observation. Day 0 is the day of tumor cell implantation, which occurred on day 7 postfertilization. F). Flow cytometric analyses of CTC from chick embryos, bearing either VHL-WT cells (marked with mStrawberry) or 1:1 VHL-WT and VHL-KO (marked with EGFP) mixed CAM tumor, harvested on day 21 post fertilization. G) Gross assessment of tumor growth in the kidneys and lungs of nude mice receiving AC-VHL-WT or a 1:1 mixture of AC-VHL-WT and AC-VHL-KO cells. H&E staining of the lung from the mixed implanted group are shown in the right panel. H) In the CAM tumor system, mixed implantation of primary tumor cells from #22 and its VHL-KO counterpart can significantly increase the metastasis in the chicken liver. I) Heatmap of the top 200 genes based on conserved gene expression patterns across comparisons of #22 VHL+ vs. VHL- cells in single cell sequencing, VHL KO vs. VHL WT ACHN models, and VHL KO vs. VHL WT RENCA models. Heatmap colors represent log<sub>2</sub> fold changes z-score scaled by column. Detailed information is listed in supplementary table 2. J) Top 30 genesets based on conserved enrichment scores across the same three comparisons are listed. Color of points represents the differential expression comparison (ACHN VHL-KO vs VHL-WT as red, RENCA VHL-KO vs VHL-WT as green, and the single cell comparison of #22-VHL+ vs VHL- as blue) and the size of the points corresponds to the adjusted p-value from GSEA, in which the bigger circles indicate up/down-regulation with lower p-values. (\*: p<0.05, \*\*: p<0.01) (not consistent with adjusted p vals in figure)

Figure 3

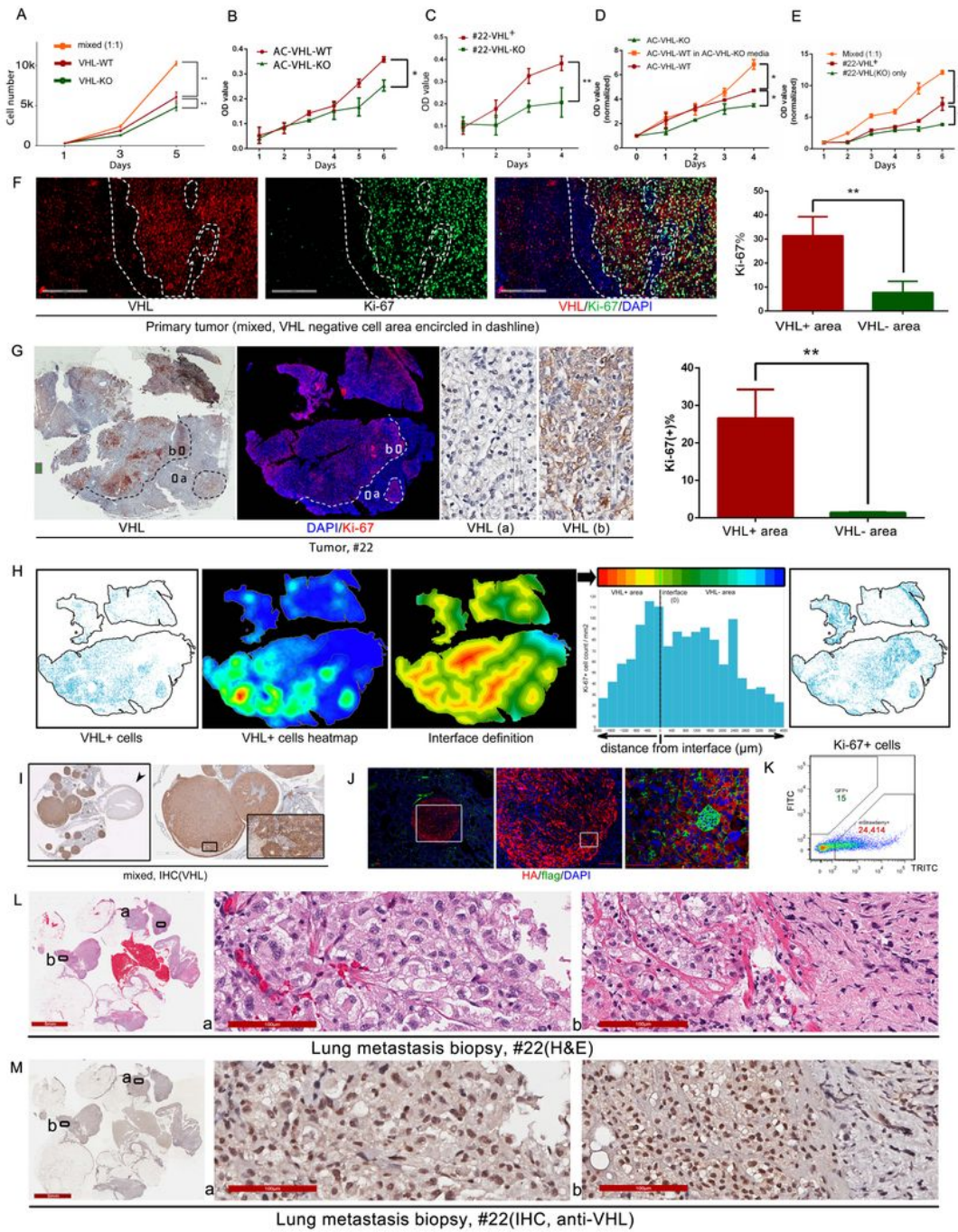


Figure 3

VHL-KO cells induce proliferation in VHL-WT cells. A) In vitro growth rate of RC-VHL-WT (red line), RC-VHL-KO cells (green line), and a 1:1 mixture of the two cells (orange line). B) In vitro growth rate of AC-VHL-KO and AC-VHL-WT cells. C) In vitro growth rate of the primary cell line from case #22 and its VHL-KO counterpart. D) In vitro growth rate of AC-VHL-WT with conditioned media from AC-VHL-KO (orange line). E) In vitro growth rate of primary cell line from case #22 when mixed with its VHL-KO counterpart. F)

A section of primary tumor derived from an implantation of 1:1 RC-VHL-KO:RC-VHL-WT cells was stained with IF to detect VHL (red), Ki67 (green), and nuclei (DAPI, blue). The dash lines demarcate VHL-negative areas with intact nuclei. G) VHL IHC and Ki-67 IF in serial sections of human ccRCC (case #22). A high-magnification image shows cytoplasmic VHL expression specifically in area (b) and not in area (a). The bar graph shows the average percentage of Ki-67 positivity in the VHL-positive and VHL-negative regions. H) The spatial relationship between VHL and Ki-67 expression in case #22 was assessed with IF. Fluorescent images were analyzed with HALO software. In the first and fifth panels, VHL-positive cells and Ki-67-positive cells are represented by blue dots. The second panel shows a heatmap of VHL-positive cell density. The third panel shows a boundary map of the VHL-positive tumor regions as topographic contour lines indicating the distance from the tumor boundary. For distance measurements of Ki67-positive cells, contour lines were placed up to 2000  $\mu\text{m}$  from the tumor edge towards the inside of the tumor and up to 4000  $\mu\text{m}$  away from the tumor edge of VHL-positive tumor regions. Regions between the contour lines are shown as different colors from the innermost red to farthest blue. Ki-67-positive cells in each region were counted, normalized to the area, and plotted in a histogram that is shown in the fourth panel. I) VHL IHC staining of the lung metastasis from the mixed implanted group with RC-VHL-WT and RC-VHL-KO cells. The arrow indicates the heart. J) IF of a small, lung metastatic nodule from a mouse implanted with the mixture with HA-positive RC-VHL-WT cells shown in red and the few flag-positive VHL-KO cells shown in green. K) flow cytometry analysis of the lung metastasis showing the relative proportion of RC-VHL-WT (TRITC+) and RC-VHL-KO(FITC+) cells. L) H&E staining and M) VHL IHC staining of the lung metastasis from the case #22. (\*  $p < 0.05$ , \*\*  $p < 0.01$ ).

Figure 4

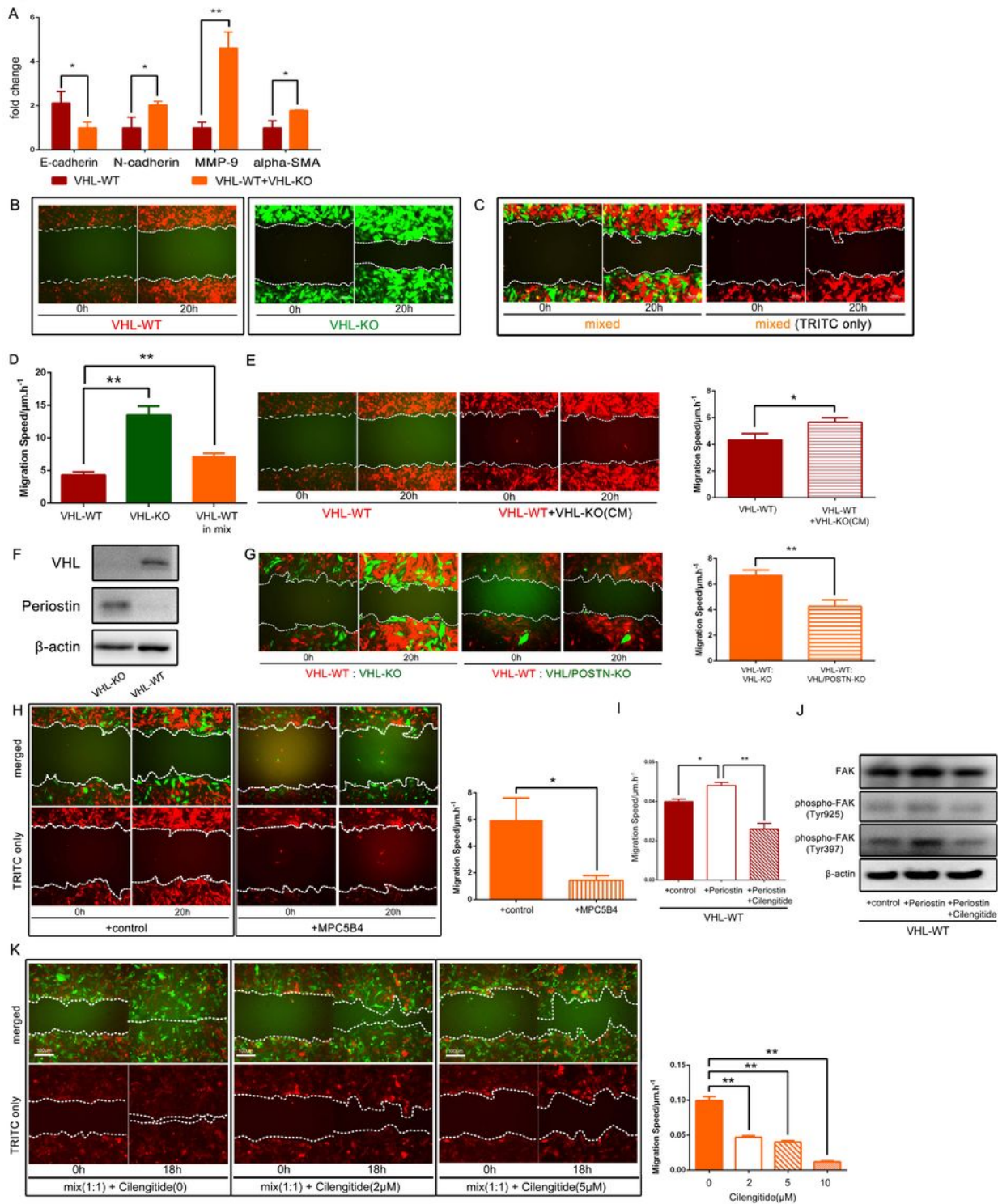


Figure 4

VHL-KO cells induce the EMT and the motility in VHL-WT cells. A) With qRT-PCR, EMT markers in RC-VHL-WT cells alone or cocultured with VHL-KO cells separated by a Transwell (VHL-WT +VHL-KO). B) RC-VHL-WT cells were marked with HA-tagged mStrawberry, and RC-VHL-KO cells were marked with flag-tagged EGFP. The motility of RC-VHL-WT, VHL-KO, and (C) a mixture of the two in a 1:1 ratio was monitored in a 2D scratch assay with time-lapse, live-cell microscopy over 20 hrs. Respective videos are in

Supplementary Video S1. (D) Quantification of the migration speed of the three cell groups is shown. E) Migration of VHL-WT cells with conditioned medium harvested 2 days after the culture of VHL-KO cells in over 90% confluence. Respective videos are shown in Supplementary Video S3. F) Western blot of VHL and POSTN protein expression in RC-VHL-WT and RC-VHL-KO cells. G) The migration speed of VHL-WT cells (mStrawberry+) cocultured with VHL/POSTN-KO cells (EGFP+) or VHL-KO cells (EGFP+) (see also Supplementary Video S5). H) Anti-POSTN mAb MPC5B4 (1  $\mu$ g/mL) was added to VHL-WT cells cocultured with VHL-KO cells. The migration speed of VHL-WT cells without and with MPC5B4 was assessed (see Supplementary Video S6). I) Migration speeds of VHL-WT cells were assessed alone and with the addition of recombinant POSTN protein with and without the further addition of the integrin inhibitor cilengitide. J) Western blot of phospho-Tyr 397, and total FAK in VHL-WT cells cultured alone and with the addition of recombinant POSTN protein with and without the further addition of the integrin inhibitor cilengitide.  $\beta$ -actin was used as a loading control. K) Scratch assay of a 1:1 mixture of VHL-WT and VHL-KO cells was assessed at 18 hours. A dose titration of cilengitide was added to the cultures (see Supplementary Video S7). (\*:  $p < 0.05$ , \*\*:  $p < 0.01$ )

Figure 5

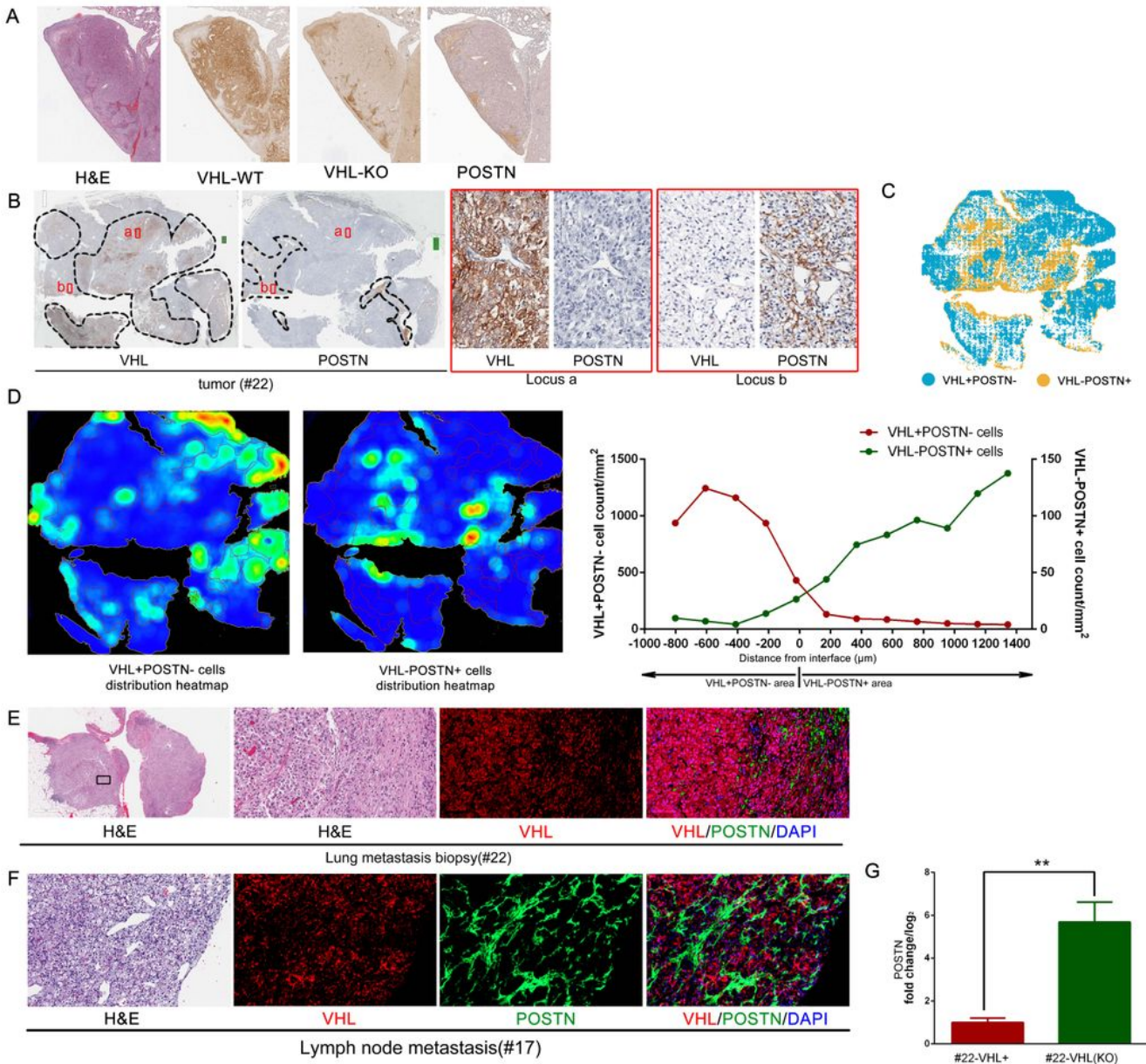


Figure 5

Periostin is a soluble factor secreted by VHL-KO cells that promotes metastasis. A) Serial sections from a large, lung metastatic lesion resulting from implantation of a 1:1 mixture of VHL-WT and VHL-KO cells were stained with H&E and IHC against HA tag (VHL-WT cells), flag tag (VHL-KO cells), and anti-POSTN. B) Serial sections of the primary tumor tissue from case #22 were stained for VHL and POSTN. Higher magnification of the boxed areas a and b are shown on the right. C) Multiplex IF stain, analyzed by HALO

software, showing the cellular distribution of VHL+ POSTN- and VHL-POSTN+ cells in case #22 primary tumor. D) Halo analysis in (C) was used to generate heatmap of VHL+ POSTN- and VHL-POSTN+ cells. Warmer colors (orange) identify areas of denser cells, and cooler colors (dark blue) signify areas with sparser cells. The rightmost plot scored the VHL+ POSTN- and VHL-POSTN+ cells in each evenly divided area with respect to the interface border of VHL+ POSTN- area. It shows VHL+ POSTN- cells (red curve, left y-axis) and VHL-POSTN+ cells (green curve, right y-axis) do not co-localized in the same area. E) The lung metastatic lesion of case #22 and F) the retroperitoneal lymph node metastatic lesion of case #17 were stained by H&E and IF to detect VHL (red), POSTN (green), and nuclei, (DAPI, blue). G) qRT-PCR analysis of POSTN in the #22-VHL+ primary cells and its VHL-KO counterpart upon CRISPR/Cas9 mediated knockout. (\*\*:  $p < 0.01$ )

Figure 6

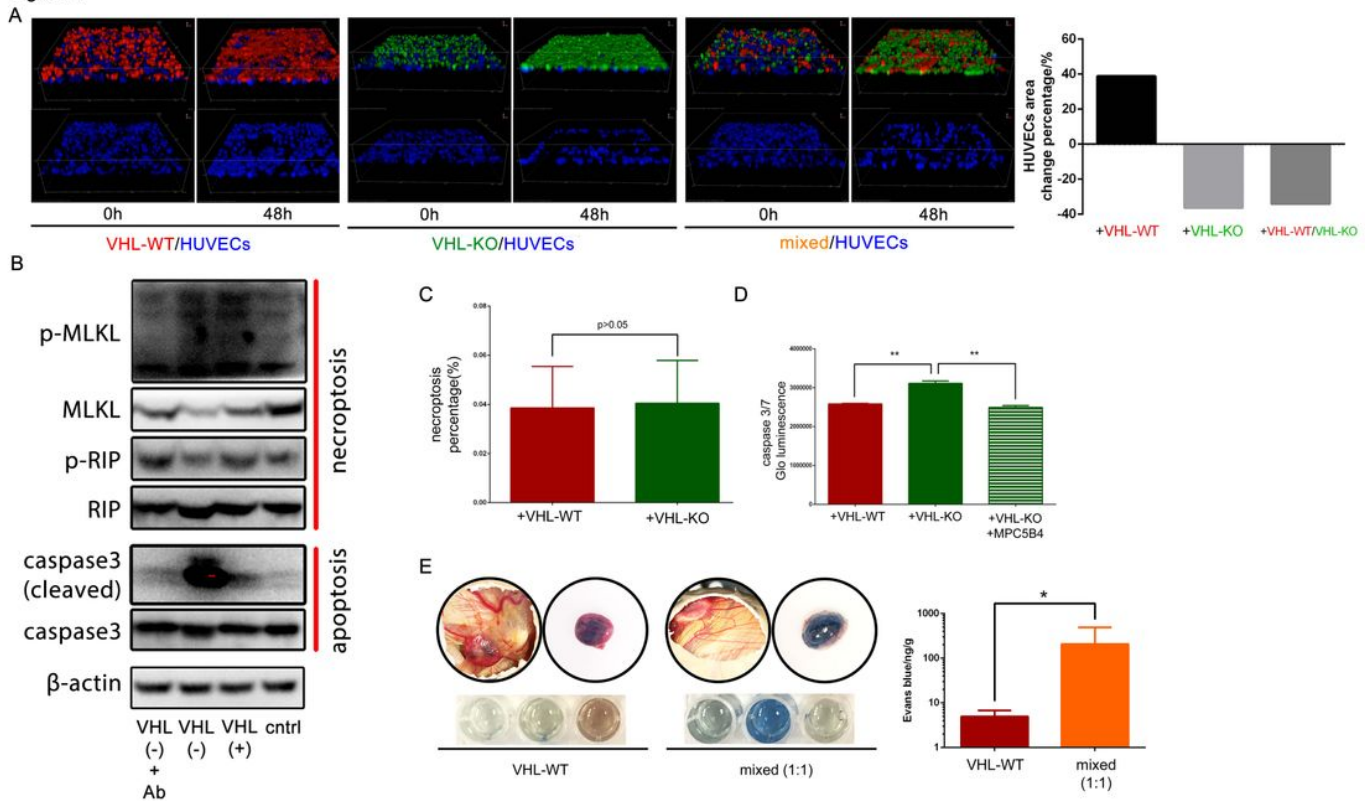


Figure 6

VHL-KO cells and POSTN cause vascular destruction that enhances intravasation. A) A 3D endothelial invasion assay was performed by placing a layer of tumor cells (either mStrawberry-marked VHL-WT cells, EGFP-marked VHL-KO cells, or a 1:1 mixture of the two cell types) over a layer of Matrigel (~ 30  $\mu$ m thick) that was above a HUVEC endothelial cell layer (marked with tagBFP). HUVEC area was assessed 48 hours after coculture (graph, right). B) HUVECs were cocultured in Transwells with VHL-WT (labeled "VHL (+)") or VHL-KO (labeled "VHL(-)") cells without or with the anti-POSTN mAb MPC5B4 (labeled "Ab"). After 48 hours of coculture, HUVEC extracts were harvested and analyzed by Western blot for necroptosis- and apoptosis-associated proteins. C) HUVECs cocultured with VHL-WT or VHL-KO cells for 48 hours were assessed for necroptosis with a reporter assay by scoring the count of EthD-III(+) cells, which was normalized to the Hoechst 33342-positive nuclei count. D) Apoptosis was evaluated with the Caspase-Glo

3/7 luminescence reporter assay in HUVECs cocultured with VHL-WT cells, VHL-KO cells, or VHL-KO cells plus 1  $\mu\text{g}/\text{mL}$  of anti-POSTN MPC5B4 mAb. E) Tumor vascular leakage was assessed with the Miles assay on CAM tumors from VHL-WT cells or a 1:1 mixture of VHL-WT and VHL-KO cells. Evans Blue dye was injected intravenously into the chick embryo. The extent of tumor vascular leakage was scored by the amount of dye that leaked into the tumor. (\*  $p < 0.05$ , \*\*  $p < 0.01$ )

Figure 7

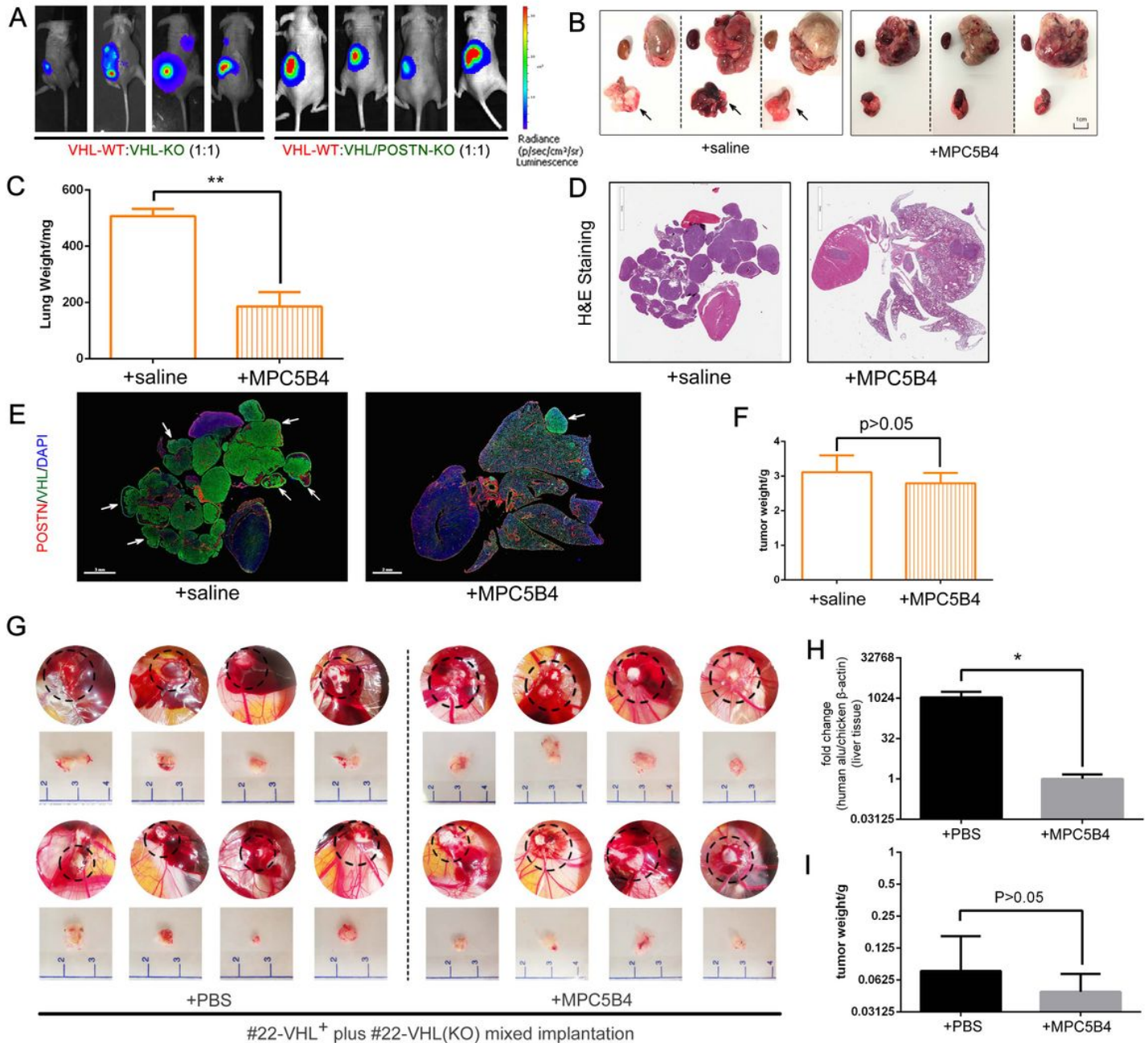
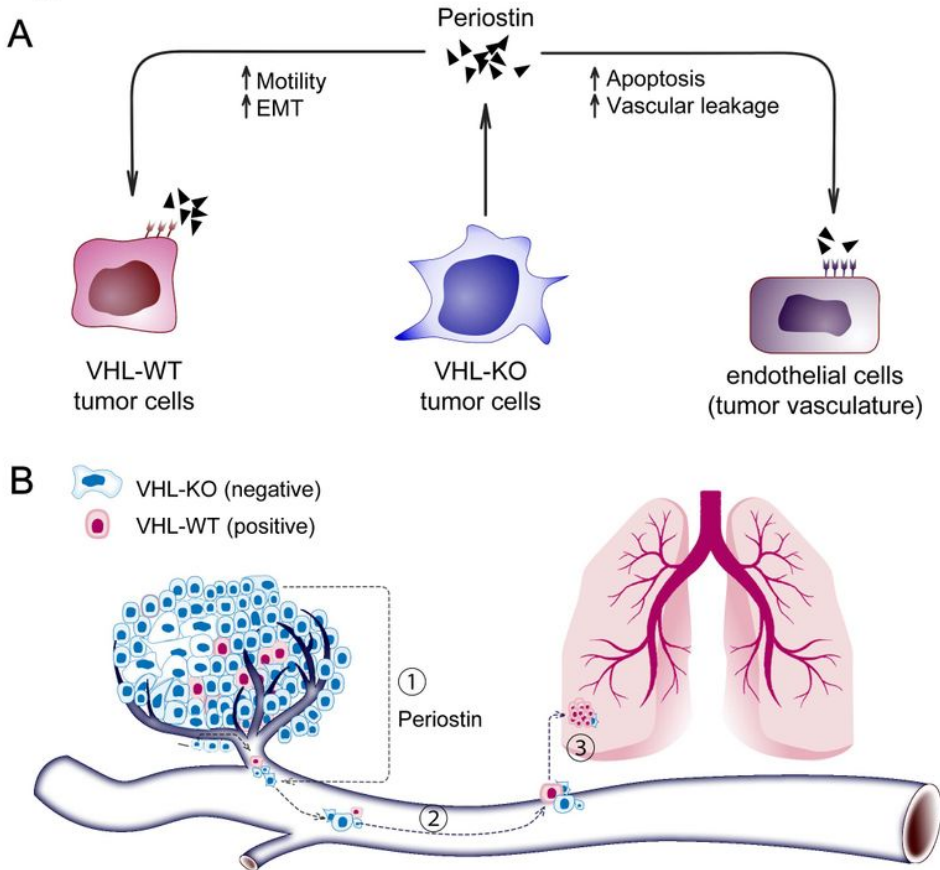


Figure 7

Inhibition of POSTN blocks metastasis in ccRCC models. A) Intrarenal co-implantation of  $1 \times 10^6$  total RC-VHL-WT cells, RC-VHL-KO cells, or a 1:1 mixture of RC-VHL-WT and RC-VHL/POSTN-KO cells. BLI at 4 weeks post implantation is shown. B) Mice that received renal implantation of a 1:1 mixture of RC-VHL-

WT and RC-VHL-KO cells were treated with either control IgG or anti-POSTN MPC5B4 mAb (n =6). Primary tumors and lungs harvested at 4 weeks post implantation are shown with lung weights (C). D) H&E stain of lung lobes and heart from control- or MPC5B4-treated tumor-bearing animals. E) IF stain for POSTN in red, VHL in green, and DAPI in blue of the same tumor sections in C. White arrows indicate selected lung metastases. F) primary tumor weights for each group are shown. G) Gross view of the primary tumor on CAM treated with either control or MPC5B4, and tumors were established from mixed implantation of primary cell line from case #22 and its VHL-KO counterpart. The qRT-PCR analysis of the chicken liver metastasis is shown in (H) and the primary tumor weight analysis is shown in (I). (\*: P<0.05, \*\*: P<0.01)

**Figure 8**



**Figure 8**

Schematic illustration of the collaborative metastasis model between VHL-KO and VHL-WT cells in ccRCC. A) A summary of the pro-metastatic paracrine functions mediated by POSTN. B) The cooperative metastatic mechanism uncovered by our model's paracrine interactions between VHL-KO and VHL-WT cells. Intravasation is shown as step 1, cell survival in the circulation is shown as step 2, and metastatic colonization is shown as step 3.

## Supplementary Files

This is a list of supplementary files associated with this preprint. Click to download.

- [Supplementarymaterialstxtonly.docx](#)
- [S4.jpg](#)
- [S6.jpg](#)
- [S5.jpg](#)
- [VideoS5.mov](#)
- [VideoS3.mov](#)
- [VideoS2.mov](#)
- [S3.jpg](#)
- [Table1.docx](#)
- [S2.jpg](#)
- [S1.jpg](#)
- [VideoS6.mov](#)
- [VideoS7.mov](#)
- [VideoS1.mov](#)
- [VideoS4.mov](#)